MASTER THESIS

MASTER OF SCIENCE IN NUCLEAR PHYSICS

Measurement of β^+ emitters production cross sections of interest for range verification in proton therapy

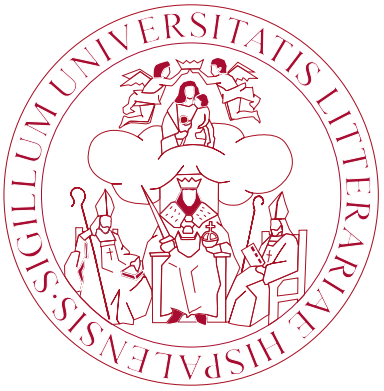

Author

Juan Saiz Lomas

Supervisors

Dr. Carlos Guerrero Sánchez

Dr. María del Carmen Jiménez Ramos

University of Seville

Faculty of Physics

—

Seville, June 2017

Acknowledgements

First of all, I would like to express my gratitude to my supervisors, Dr. Carlos Guerrero and Dr. María del Carmen Jiménez, for giving me the opportunity to develop this research proyect and for supporting me through its entire duration. I could always count on immediate and certainly valuable help from them at any moment. Besides that, their guidance and encouragement has made me improve my knowledge and experimental skills as an experimental nuclear physicist.

In addition, I would also like to thank all of the staff working at CNA and everyone who has collaborated in the accomplishment of the experiments. Among them, I would particularly like to thank Dr. Javier García, Miguel Macías, Andrés Gómez, Jorge Lerendegui, and the PET/CT scanner group, especially Ángel Parrado.

Juan Saiz.

Abstract

The uncertainty in the dose curve delivered during the treatment of tumors with protons, *i.e.* the position of the Bragg peak, makes it necessary to apply safety margins from 1% to 3% in the beam range. This means nearly 1 cm in a 30 cm deep tumor, which certainly limits the benefits of having a sharp Bragg peak. Reducing this uncertainty would allow a reduction of the treatment volume and thus result in a better utilization of the advantages of protons compared to conventional radiotherapy.

Among the different techniques that are being proposed for range verification, some of which have already been clinically tested), the measurement of the distribution of β^+ radioactive nuclei (known as PET isotopes) produced by the proton beam along its path allows detecting variations of only a few millimeters in the proton beam range. For this purpose, a better database of production cross sections of β^+ emitters as function of the energy of the incident proton for a wide range of elements present in the body (mainly C, O, N, P and Ca) is needed, specially in the low energy range (up to 20 MeV). This applies, among others, to the commonly used long-lived PET isotopes ^{11}C and ^{13}N.

The objective of this work is to measure the production cross sections of ^{11}C and ^{13}N in C, O and N at different energies from 7 to 18 MeV. For this purpose, stacks of targets containing these elements have been irradiated with the 18 MeV proton beam of the CNA cyclotron, and the 511 keV photons emitted in the annihilation of the positrons from the β^+ decays of the isotopes of interest have been measured. This measurement was performed both with NaI(Tl) scintillator detectors and a PET/CT system.

A total of six reaction cross sections have been sucessfully measured with uncertainties in the order of 15-20%. These have been compared to the data available in EXFOR showing an overall good agreement regarding the ^{16}O(p,*)^{13}N and ^{14}N(p,*)^{11}C reactions, and sizable differences in the case of the other reactions. Last, a series of improvements for future measurements have been identified and discussed.

Contents

List of Figures

List of Tables

1 Introduction and Objectives

1.1 Proton therapy

The history of proton therapy began in 1946 when Robert Wilson published a paper in which he proposed to use accelerator-produced beams of protons to treat deep-seated tumors in humans [1, 2]. Further progress was made in 1954 when the first human was treated with proton beams at the Lawrence Berkeley Laboratory [3]. Later in 1962, specialized radiosurgical proton treatments started to take place at the Harvard Cyclotron Laboratory [4, 5], followed in the mid 1970s by treatments for ocular cancers [6] and larger tumors [7].

Nowadays, according to the Particle Therapy Co-Operative Group (PTCOG) [8], there are 63 proton therapy centres in operation and 40 under construction and expected to be treating patients before the end of 2019. There has been a total of 131240 patients treated (1954-2015) and the number is only increasing with time (Figure 1).

The possibility of localizing high dose rates at the tumor while minimizing it in the surrounding healthy tissue has made of proton therapy a very advantageous therapy for treating some specific tumors compared to other types of radiotherapies.

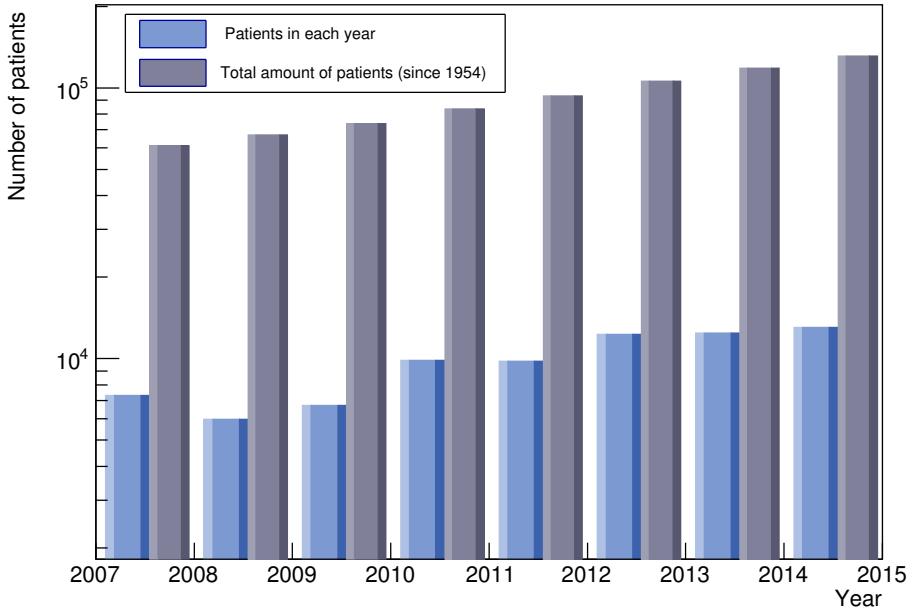

Figure 1: *Total number of patients treated with proton therapy since 1954 and each year (data provided by PTCOG).*

1.2 Physics principles of Proton therapy

Proton therapy is a type of external beam radiotherapy that uses a proton beam to irradiate diseased tissue, most often in the treatment of tumors.

In this treatment, protons are accelerated until reaching energies in the range of 70 to 250 MeV: the greater the proton energy, the greater depth reached. Therefore, the energy of the incident protons depends on the depth of the diseased cells to be targeted. When the protons deposit high dose in these cells, they damage their DNA, ultimately killing them or stopping their reproduction. The main advantage of protontherapy compared to other external radiotherapy techniques is the possibility of localizing higher dose (energy deposited per unit of mass) at the tumor while considerably reducing it in adyacent tissues. This is possible because the dose delivered to tissue is maximized over the last few millimeters of the particle's range. This maximum is called the Bragg peak and it is shown in Figure 2. However, since the goal in clinical practice is to irradiate the entire tumor with an homogenous dose, protons with different energies and Bragg peaks at different depths are applied. The combination of these multiple Bragg peaks results in the so called *spread-out Bragg peak* (SOBP), also shown in Figure 2.

The origin of the Bragg peak, hence the main adventage of proton therapy compared to other techniques, lies in the particularities of the interaction of charged particles (in this case protons) with matter. There are different ways in which a proton can interact in matter [1]:

- Coulombic interactions with atomic electrons.
- Coulombic interactions with the atomic nucleus.
- Nuclear reactions.
- Bremsstrahlung.

To a first-order approximation, in terms of energy loss, the main interaction is the continuous kinetic energy loss via frequent inelastic Coulombic interactions with atomic electrons. This energy loss determines the range of the proton beam in a patient. Since the mass of the proton is 1832 times greater than the mass of an electron, proton's trajectories remain unaltered by collisions with the electrons and thus protons travel in a nearly straight line. However, a proton in the vicinity of an atomic nucleus experiences a repulsive elastic Coulombic interaction which, owing to the large mass of the nucleus, deflects the proton from its original straight-line trajectory. Furthermore, non-elastic nuclear reactions between protons and the atomic nucleus are

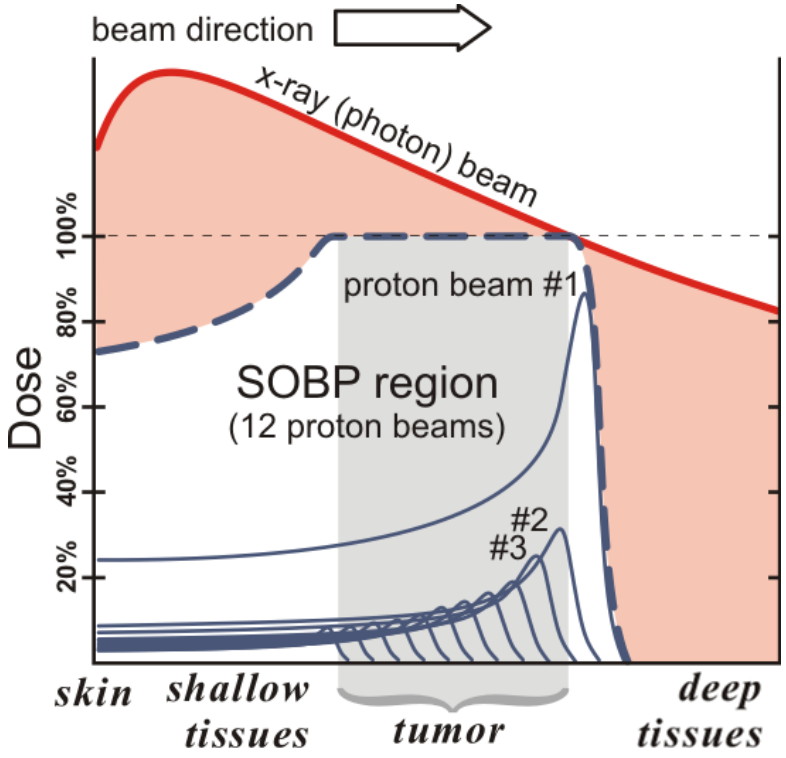

Figure 2: *Cualitative comparison between proton and x-ray dose distributions. It is shown how high dose rates can be achieved in the tumor with lower rates in adyacent tissue by protons using diferent energy-depth proton beams making a SOBP.*

less frequent but still possible. As it will be shown later, the products of these nuclear reactions can be used for proton range verification. Finally, Bremsstrahlung is theoretically possible but at therapeutic proton beam energies is negligible.

A physically complete theory was developed by Bethe [9] and Bloch [10] regarding the energy loss rate of charged particles in matter taking quantum mechanical effects into consideration. The average rate at which a charged particle with energy E loses energy dE per unit path length dx is described by the *linear stopping power* (S), which can be expresed in terms of the Bethe-Bloch formula as

$$\frac{S}{\rho} = -\frac{1}{\rho}\frac{dE}{dx} = 4\pi N_A r_e^2 m_e c^2 \frac{Z}{A}\frac{z^2}{\beta^2}\left[\ln\frac{2m_e c^2\beta^2\gamma^2}{I^2} - \beta^2 - \frac{\delta}{2} - \frac{C}{Z}\right] \tag{1.1}$$

where ρ is the density of the absorber material, N_A is Avogadro's number, r_e is the classical electron radius, m_e is the mass of an electron, c is speed of light, z is the charge of the projectile, Z is the atomic number of the absorbing material, A is the atomic weight of the absorbing material, $\beta = v/c$ where v is the speed of the projectile, $\gamma = (1-\beta^2)^{-1/2}$, I is the mean excitation potential of the absorbing material, δ is the density corrections arising from the

shielding of remote electrons by close electrons and will result in a reduction of energy loss at higher energies, and C is the shell correction item, which is important only for low energies where the particle speed is near the velocity of the atomic electrons.

Moreover, the *absorbed dose* (D), defined as the average energy $d\epsilon$ imparted by ionizing radiation to matter per unit mass (dm), can be related to the previously defined energy loss rate (and therefore the stopping power) under some assumptions by [11],

$$D = -\frac{d\epsilon}{dm} \simeq \frac{\Phi}{\rho}\frac{dE}{dx}, \tag{1.2}$$

where Φ is the primary particle fluence. To a first order approximation, the average energy loss rate, and thus the dose absorbed, increases with the proton energy loss as $1/\beta^2$. The stopping poweer increases with the residual energy of the particle (instantaneous energy of the particle retained by it as it travels through the material). Hence, as the particle looses energy it causes more and more ionization along its paths until it reaches the highest absorbed dose point known as Bragg peak. After that point the particles have lost almost all of their energy and get quickly neutralized by atracting electrons from their surrondings.

1.3 Range verification in protontherapy

A magnitud of great interest for protontherapy is the range. Range is defined as the depth at which half of the particles (protons in this case) incident in the absorber have come to rest. This is inherently an average quantity defined for a beam and not for individual particles. If protons are considered to loose energy continously and straigh ahead (negglecting lateral scattering), the range can be calculated by

$$R = \int_0^E \left(\frac{dE'}{dx}\right)^{-1} dE', \tag{1.3}$$

Figure 3 shows an example of the fraction of initial fluence of protons as a function of depth in water for a 160 MeV proton beam. This curve features two well diferentiated regions: a first one where there is a gradual deplection from entrance to near the end of range, and a rapid falloff at the end. The first is caused by nuclear reactions of protons with atoms in the medium (difference between the solid line and the dotted line), and the latter is caused by protons being stopped. The stochastic fluctuations in the energy loss and the range straggling of individual protons lead to a sigmoid shape of the distal falloff. Together with the fraction of initial proton fluence as a function of depth in water, the relative dose curve is displayed (dashed line). Here we can see how the maximum dose deposition corresponds to the last few milimeters of the range, forming the Bragg peak.

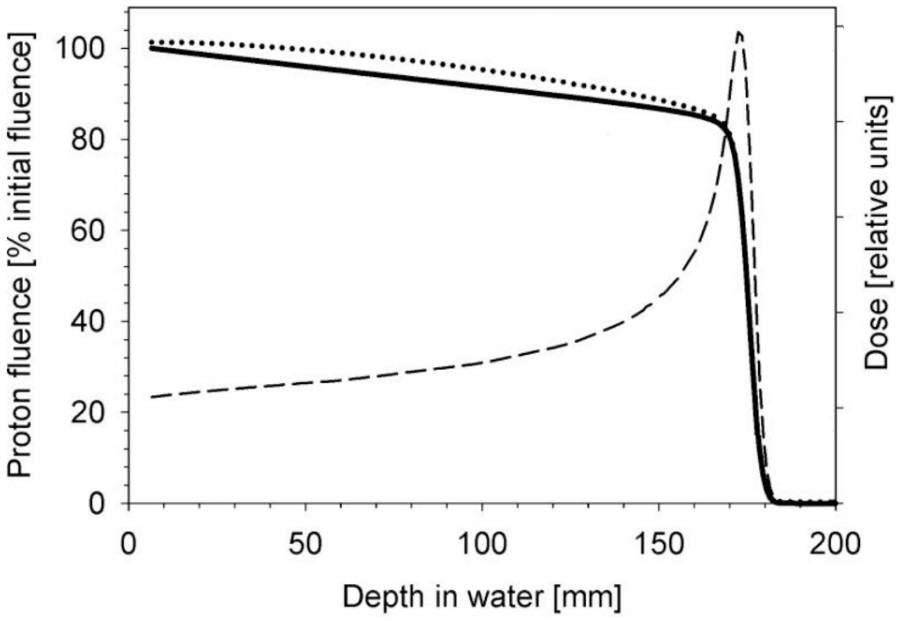

Figure 3: *Example of the fraction of the fluence Φ in a broad beam of 160 MeV protons (in arbitrary units) as a function of depth z in water [12] (see text for details).*

As mentioned before, most protons in matter travel almost in a straight line. That is to say that on average, the proton's pathlength is nearly equal to its projected pathlength and range. The finite range of this proton beam, together with the fact that the most of the dose is delivered at the end of it, is one of the main adventages of proton therapy compared to conventional radiotherapy. However, in order to fully exploit these physical advantages, knowledge of the exact location of the energy deposition in tissue is mandatory. If the proton range is not accurately known, severe underdosage in the tumor, leading to bad tumor control, or overdosage in the surrounding healthy tissue, leading to side effects of the therapy, is possible [11]. In fact, there are still considerable uncertainties caused by imaging, patient positioning, beam delivery and dose calculation. The uncertainty in the dose curve delivered during the treatment with protontherapy makes it necessary to apply safety margins from 1% to 3% [13], this means nearly 1 cm in a 30 cm deep tumor, which certainly limits the benefit of having a sharp Bragg peak. Reducing the uncertainties would allow a reduction of the treatment volume and thus result in a better utilization of the advantages of protons. The range verification (or monitoring) can be achieved by looking at signatures of the beam interaction, such as the products of the nuclear reactions of protons along their path through the patient's body [14].

These can be charged particles, neutrons or photons exiting the body. In the case of photons,

these can be emitted prompt as a result of the de-excitation of reactions products, or delayed from unstable nuclei resulting from nuclear reactions that decay after the irradiation. Range verification from the detection of prompt photons is based either in the study of the depth profile or on the time profile, both related to the dose depth profile of interest. In the case of delayed photon emission, PET-like detectors are used to detect β^+ decay rates as function of the depth profile shortly after the irradiation.

Range verification via the detection of PET isotopes (for instance ^{15}O) has already been clinically tested and validated [15], but there is room for improvement on: detection systems, simulations, and nuclear physics input data. The latter refers to a better database of production yields of β^+ emitters as function of energy (up to 250 MeV) of the incident proton for a wide range of elements present in the body (mainly carbon, oxygen, nitrogen, phosphorus and calcium). This applies to the commonly used (long- lived) PET isotopes ^{11}C, ^{13}N and ^{15}O. But the need for improved production yields is maybe more urgent in the case of short-lived PET isotopes like ^{10}C, ^{12}N, ^{29}P or ^{38m}K, for which very few data are available.

1.4 Objetives

The objective of this work is the development of the experimental, simulation and analysis tools needed to measure production cross sections of PET isotopes for range verification in protontherapy. These are to be applied in a first phase to the production of ^{11}C and ^{13}N in $^{\text{nat}}$C, $^{\text{nat}}$O and $^{\text{nat}}$N for protons below 18 MeV at the CNA cyclotron. The activity measurements will be perfomed with two different detection set-ups, a NaI detector and a PE/CT scanner, in order to validate the use of any of them for measurements at other facilities when higher energies are to be explored.

This project should continue with a more accurate measurement of the production cross sections of the mentioned isotopes, at these and higher energies, and also in the measurement of a wider variety of PET isotopes including ^{15}O, ^{10}C, ^{12}N, ^{29}P or ^{38m}K.

2 Current status of production yields of β^+ (PET) isotopes for range verification

2.1 Status of experimental production yields: data availability

The number of positron-emitting radionuclides is large. However, for routine PET investigations, mainly the short-lived "organic" positron emitters, ^{11}C and ^{18}F , and to a less extent ^{15}O and ^{13}N, are used.

Regarding range verification in proton therapy, there are only a few elements present in clear mayority in the human body, and therefore only a few positron emitters to be produced via proton induced nuclear reactions. These and their approximate abundances are: Oxygen (65,0%), Carbon (18,0%), Hydrogen (10,0%), Nitrogen (3,0%), Calcium (1,4%), Phosphorus (1,1%), Potassium (0,2%) and others (1,3%).

From these isotopes, this work is focused on the measurement of the production yields of the β^+ emitters produced via proton induced nuclear reactions in the three more abundant elements, namely ^{nat}O, ^{nat}C and ^{nat}N, since no PET-isotopes are produced in reactions with Hydrogen. The positron emitters that can be produced from these natural elements are ^{11}C,

Element	Isotopes	Reactions	β^+ emitter	Previous measurements
^{nat}C	^{12}C (98,9%)	^{12}C(p,pn)	^{11}**C**	[16] [17] [18] [a,b]
		^{12}C(p,γ)	^{13}**N**	[19][a,c]
	^{13}C (1,1%)	^{13}C(p,t)	^{11}**C**	[20][a]
		^{13}C(p,n)	^{13}**N**	[20] [21] [22] [b,d]
^{nat}O	^{16}O (99,8%)	^{16}O(p,3p3n)	^{11}**C**	[20] [23] [a,b,c]
		^{16}O(p,2p2n)	^{13}**N**	[20][23][24][d]
^{nat}N	^{14}N (99,6%)	^{14}N(p,2p2n)	^{11}**C**	[24] [25] [d]
		^{14}N(p,pn)	^{13}**N**	[25] [26] [b]

[a] Few or none measurements below 18 MeV

[b] Disagreement between some measurements at some ranges

[c] Few measurements all range

[d] Good data and/or evaluation

Table 1: *Relevant cross section and production yield data for ^{13}C y ^{13}N in a range from 0 to 20 MeV (data from EXFOR [27]).*

^{13}N and ^{15}O whose measurement needs regarding cross sectional data has shifted now to the low energy range [28]. ^{15}O has been excluded from this work because its short half-life requieres another experimental approach.

Table 1 shows a brief summary of the data availability of the main cross sections or production yields measured so far for ^{11}C and ^{13}N. Here one can see how there are some reactions that have been sufficiently measured, *e.g.* ^{16}O(p,2p2n)^{13}N or ^{14}N(p,2p2n)^{11}C (for which the IAEA has provided a recommended cross section), and others that almost have not been, *e.g.* ^{12}C(p,γ)^{11}C, ^{13}C(p,t)^{13}N, ^{13}C(p,n)^{11}C, etc. On the other hand, reactions such as ^{15}N(p,2p3n)^{11}C and ^{15}N(p,p2n)^{13}N (together with those derived from the least abundant isotopes of oxygen) have been excluded from this study since their contribution to the total cross section scaled by their relative abundance (according to the few data avaliable) are neglectible.

2.2 Status of experimental production yields: measuring techniques

Concerning the techniques used to measured the previously mentioned production yields, there is a certain variety in the methods used. The differences between experiments can be grouped in the following way:

- Particle accelerators.
- Targets.
- Reaction products and detectors.

For this kind of expeirment, the authors have used a wide variety of particle accelerators such as Tandem Van de Graaf (TVDG), clyclotrons, syncrotrons, etc. However mainly TVDG and cyclotrons have been used for low energies. The main difference regarding these experiments is that in the former, the beam energy can be selected, whereas in the latter it is given. This means that in order to measure at different energies with a cyclotron, one has to degrade the beam with different materials (moderators) and, as it will be shown later, the greater the degradation is the larger the uncertainty in the proton energy.

Author	Reaction	Accelerator	Target	Meas. type	Detector
K. Kettern, 2004	$^{nat}C(p,*)^{11}C$ $^{14}N(p,2p2n)^{11}C$	Cycl.	Target stack	Activation	HPGe
K. Matsushita et al. 2016	$^{12}C(p,pn)^{11}C$	Cyclotron (70 MeV)	HDPE	Activation	PET detector
N. M. Hintz et al. 1952	$^{12}C(p,pn)^{11}C$	Cyclotron (100 MeV)	PE	Activation	Geiger-Müller (relative measurement to *Aamodt et al.*)
Aamodt et al. 1952	$^{12}C(p,pn)^{11}C$	Cyclotron (340 MeV)	Polystyrene	Activation	Geiger-Müller
Cohen et al. 1955	$^{12}C(p,\gamma)^{13}N$	Cyclotron (22 MeV)	Enriched ^{12}C	Activation	-
Kitwanga et al. 1989	$^{13}C(p,t)^{11}C$ $^{13}C(p,n)^{13}N$ $^{16}O(p,3p3n)^{11}C$ $^{16}O(p,2p2n)^{13}N$	Cyclotron (30 MeV)	Enriched solid ^{13}C Enriched ^{16}O gas	Activation	NE102 plastic scintillators and XP2020 photomultipliers
Firouzbakht et al. 1991	$^{13}C(p,n)^{13}N$	TVDG (19 MeV) and Cyclotron (30 MeV)	Enriched solid ^{13}C	TOF	Picker NaI(Tl)
T. Akagi et al. 2013	$^{16}O(p,3p3n)^{11}C$ $^{16}O(p,2p2n)^{13}N$	Cyclotron (80 MeV)	Gelatinous water	Activation	PET detector
Z. Kovács et al. 2003	$^{14}N(p,2p2n)^{11}C$ $^{16}O(p,pn)^{13}N$	Cyclotron (20 MeV)	N_2 gas	Activation	HPGe detector
M. Sajjad et al. 1986	$^{16}O(p,2p2n)^{13}N$ $^{16}O(p,pn)^{13}N$	TVDG (16 MeV)	2% NO_2 in O_2	Activation	NaI(Tl) detector

Table 2: *Summary of the different reactions measured and methods used in previous measurements.*

There have also been used many different types of targets for the measurement of ^{11}C and ^{13}N in Carbon, Oxygen and Nitrogen. Although mainly graphite or polyethylene has been used for the reactions induced in Carbon, also highly enriched targets have been used to separate the ones in ^{12}C and ^{13}C. Regarding Oxygen and Nitrogen, there is an even wider assortment of possible targets, since both solid and gaseous targets can be used (*e.g.* gelatinous water or O_2 targets for Oxygen, or polyamydes or N_2 targets for the Nitrogen).

Finally, either the diferent products of the proton induced reactions or the double 511 keV γ-rays produced in the β^+ decay can be measured. Many of the production yields mentioned in the previous section have been measured focusing on the neutron production of the reactions via the time of flight (TOF) technique. Alternatively, in the experiments in which the target activation has been measured, Geiger-Müller counters or scintillator detectors have been used to measure the positrons or the 511 keV photons, respectively, exiting the target.

The two methods mentioned above do not provide necesarily the same cross section values. For instance, if one measures the ^{16}N(p,2p2n) cross section by activation (*i.e.* the magnitude of interest for range verification), one is missing the fraction of reactions in which the resulting ^{13}N is produced in a highly excited state that is unstable via particle emission. But this would not be missed if one measures this cross section by detecting the neutrons emitted in the reaction. Table 2 is a summary of the different data avaliable in EXFOR and the method (accelerator, targets and detectors) used in each one.

2.3 Production yield needs

Figure 4 contains and summarizes the different data and IAEA evaluations avaliable in EXFOR (see Tables 1 and 2) for the production yield of β^+ emitters. In view of these data, it can be seen that not all the range is covered and some measurements differ significantly from each other. A detailed study is ongoing to understand what data (energy and target element) are more important to be measured to improve the calculations of the expected activity as funtion of depth for range verification. In the mean time, in a first set of experiments at CNA we have tried to measure the cross section production for of both ^{11}C and ^{13}N in ^{nat}C, ^{nat}N and ^{nat}O using a new technique that allows measuring at several energies simultaneously in a single irradiation with a cyclotron. The comparison of the results with previosly available data, when there are, should help assessing the acuracy and validity of this new technique, as well as possible improvements.

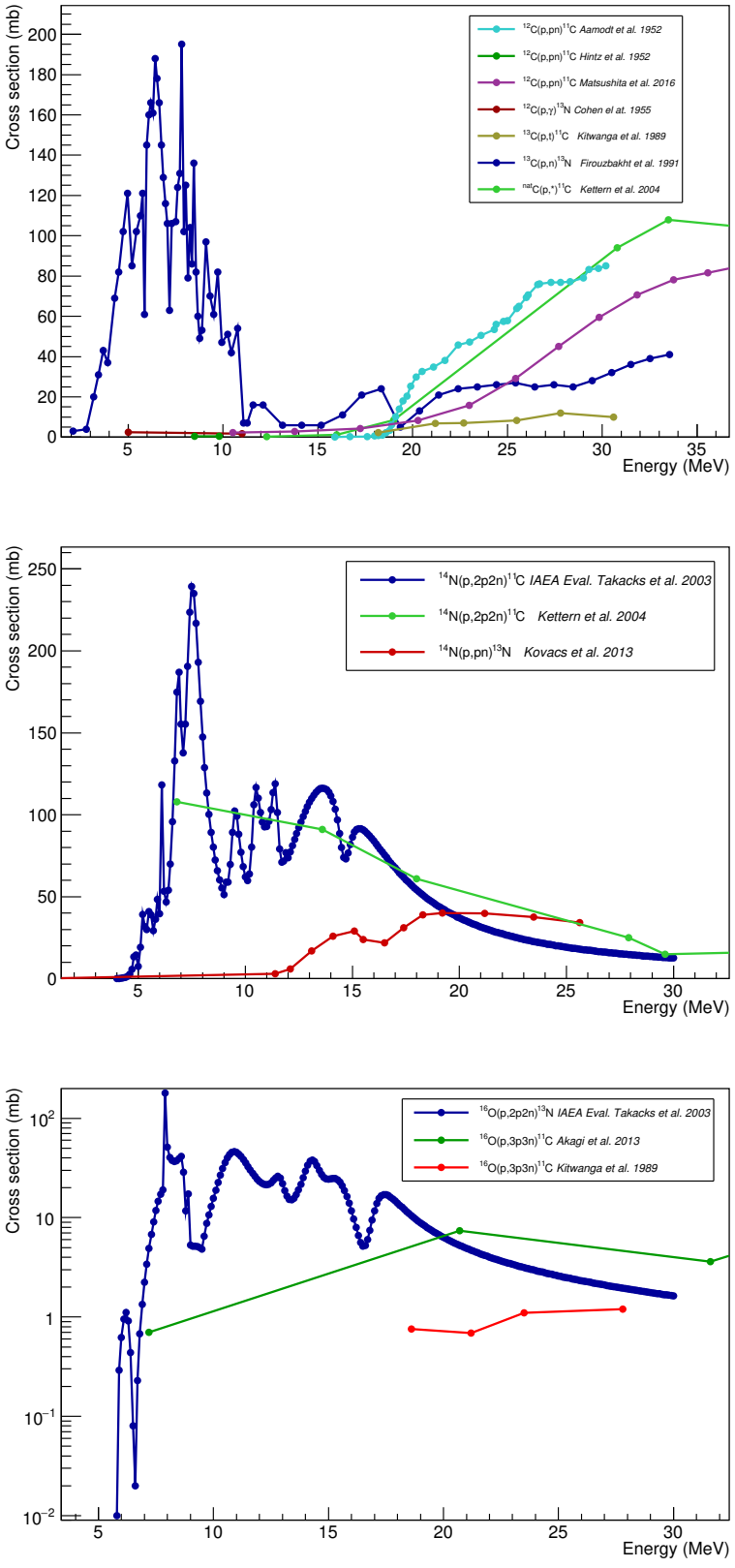

Figure 4: *(Top)* ^{11}C *and* ^{13}N *avaliable production cross section data in* ^{12}C *and* ^{13}C. *(Middle)*^{11}C *and* ^{13}N *avaliable production cross section data in* ^{14}N. *(Bottom)*^{11}C *and* ^{13}N *available production cross section data in* ^{16}O.

3 Experimental set-up for irradiation and detection

3.1 The CNA's 18 MeV proton cyclotron external beam line

The National Centre of Accelerators ("Centro Nacional de Aceleradores", CNA) [29] is a scientific research center part of the University of Seville, the "Junta de Andalucía" and the Spanish National Research Council ("Consejo Superior de Investigaciones Científicas", CSIC). This is a scientific-technical facility dedicated to interdisciplinary research. There are three particle accelerators at CNA: a 3 MV Van de Graaff Tandem, a Cyclotron providing protons and deuterons, and a 1 MV Cockcroft-Walton Tandem accelerator used for mass spectrometry.

For this work the cyclotron facility and its external beamline were used. The cyclotron (Figure 5) is a particle accelerator in which ions are accelerated through the combined application of an electric and a magnetic field. It was manufactured by Ion Beam Applications (IBA, Belgium) and it provides 18 MeV protons and 9 MeV deuterons. The extracted maximum beam intensities in the internal target ports are 80 μA ± 10% and 35 μA ± 10% for protons and deuterons, respectively.

Figure 5: *The cyclotron inside the bunker.*

Carbon foil strippers turn the beam into positive just before reaching one of the eight target ports of the cyclotron, seven of which are dedicated to short half life radioisotopes production for Positron Emission Tomography (PET) studies. The eighth exit port is used for beam transport to the research beam line, which is divided into two sections (Figure 6). The first one is inside the cyclotron vault and includes a series of remote control permanent elements to monitor and

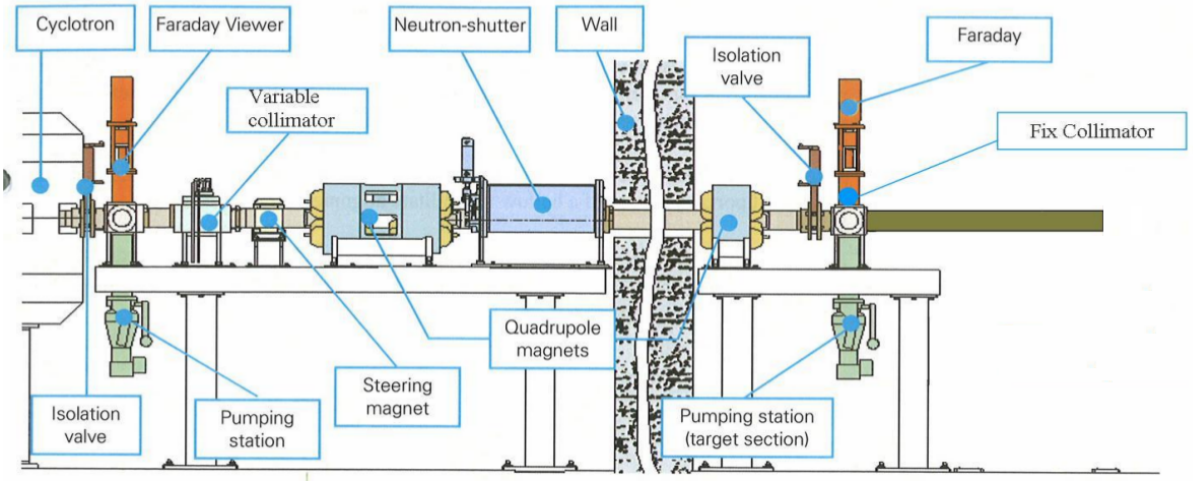

Figure 6: *Scheme of the cyclotron transport line from inside the bunker to the outer experimental area.*

to define the beam current and size, like a retractable graphite Faraday cup, a variable graphite slit (maximum aperture 15 x 15 mm), a XY set of magnetic steerers and a doublet quadrupole. Moreover, there is a neutron shutter to protect the downstream section of the unused beamline from radiations originated in the cyclotron vault. The second section is separated from the first vault by a two meters thick wall and can be isolated for pumping/venting purposes by a pneumatic valve. It contains a single quadrupole, a 15 mm diameter water cooled Al fixed collimator, a pumping station and another retractable graphite faraday cup with a phosphor scintillator (ZnS:Ag) to observe the beam shape and size by means of a video camera.

All these elements are part of a simple but versatile external beam, recently installed to perform experiments in air. It is important to highlight that the exit flange is internally covered with a 5 mm thick carbon plate to avoid its activation. Several nozzles with different sizes are available, where diverse materials windows can be adapted, and where it is possible to accommodate graphite collimators with various hole diameters.

3.2 Design of the irradiation set-up and optimization via Geant4 simulations: targets thicknesses

In order to measure production yields of ^{11}C and ^{13}N in Carbon, Nitrogen and Oxygen, materials that include these elements are needed. For this reason, due to their composition and easy availability, polyethylene (PE), poly-methylmethacrylate (PMMA) and Nylon-6-Polyamide were chosen as target materials, all supplied by Goodfellow.

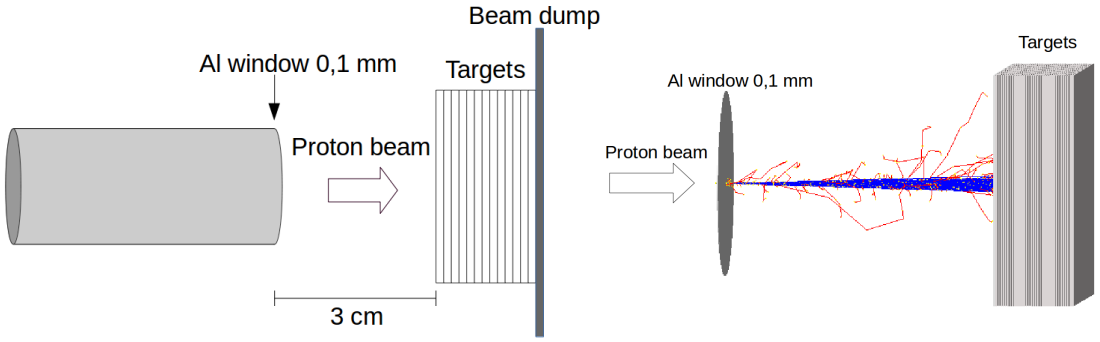

Figure 7: *Scheme of the irradiation set-up (left) and the corresponding Geant4 simulation (right).*

Material	Density (g/cm^3)	Composition	Thickness (µm)	Max. targets
PE	0,96	$(C_2H_4)_n$	200	13
PMMA	1,18	$(C_5O_2H_8)_n$	250	8
Nylon-6	1,13	$(C_6H_{11}NO)_n$	100	20

Table 3: *Materials and thicknesses chosen for the different targets for the experiment.*

The irradiation set-up consists in placing a stack of targets in front of the proton beam so that the activation of each target provides a value of the production yield at a specific energy. A scheme of the irradiation set-up is displayed in Figure 7 (left). This consists of the proton beam in vacuum passing through a 100 µm Alluminium window at the exit of the external beam line, 3 cm of air, a certain number of targets and a Graphite beam dump.

Once the materials have been chosen, it is necessary to determine how many layers are to be placed in front of the beam and what thicknesses should they have. The number of targets is equivalent to the number of energy points in which the production yield is measured and the thickness provides the energy resolution. The total thickness of the stack of targets has been chosen so that it is shorter than the range of the 18 MeV proton beam; in this way all protons traverse the stack and are stopped at the beam dump, where the beam current is measured. In addition, the thicknesses of the targets were chosen to be as small as possible without making them difficult to manipulate and always within the thicknesses avaliable provided by the supplyer. Furthermore, the targets needed to be large enough to cover the whole beam profile and for this reason, they were chosen to as squares of 25 mm side.. Table 3 contains a summary of their composition and the thicknesses chosen for the experiment.

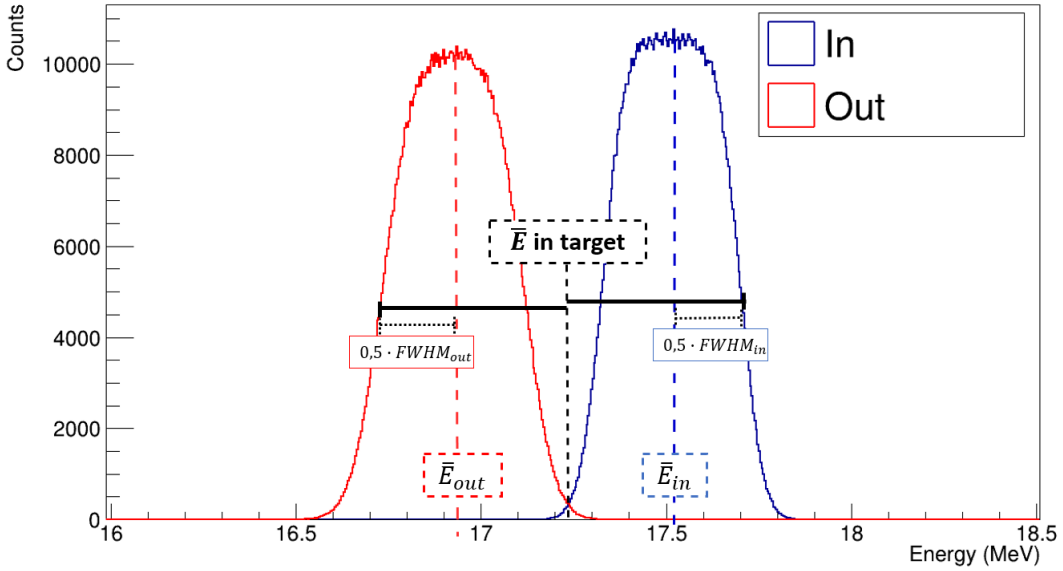

Figure 8: *Example of the proton energy distribution at entering and exiting the first PE target.*

In order to determine the maximum number of targets and the energy of the protons inside them, a simulation was performed with the Geant4 simulation toolkit. Geant4 [30], which stands for GEometry ANd Tracking, is a set of open source libraries ("toolkit") developed in C++ for the Monte-Carlo simulation of the interaction of particles with matter. Figure 7 (right) illustrates the geometry implemented in the simulation. The aim of this simulation was to obtain the energy distribution of the protons at the entrance and exit of each target, as an estimate of the range mentioned above.

The average energy inside each target was obtained by

$$\overline{E} = \frac{\overline{E}_{\text{in}} + \overline{E}_{\text{out}}}{2} \tag{3.1}$$

and the lower and higher errors by

$$\delta E_{low} = \frac{FWHM_{\text{out}}}{2} + \frac{\overline{E}_{\text{in}} - \overline{E}_{\text{out}}}{2} \tag{3.2}$$

and

$$\delta E_{high} = \frac{FWHM_{\text{in}}}{2} + \frac{\overline{E}_{\text{in}} - \overline{E}_{\text{out}}}{2} \tag{3.3}$$

respectively. Figure 8 illustrates the proton energy distribution entering and exiting the first PE target as an example.

The simulation was validated for several cases with SRIM-2013 [31]. SRIM-2013 is a freely distributable code that calculates, using the Monte-Carlo method, the energy loss and change

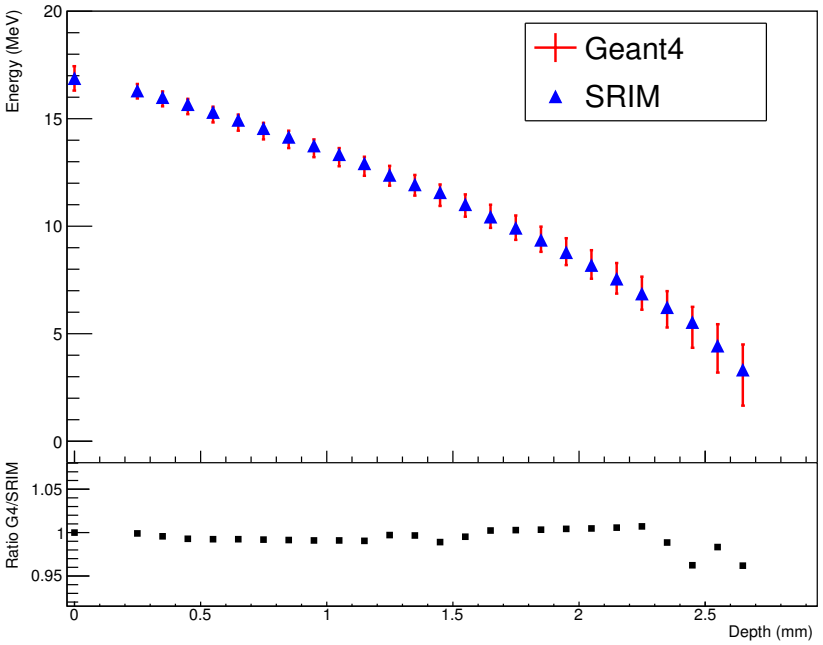

Figure 9: *Example of the validation of the Geant4 simulation with SRIM for one PMMA (250 µm) target and 25 Nylon-6 targets (100 µm).*

of direction of ions as they traverse matter. For this purpose, it employs a treatment of the interatomic potential adjusted to quantum mechanical calculations to describe the ion-atom collision (understanding ion as a projectile and the atom as the target).

As an example, Figure 9 represents the proton energy inside a target stack made of PMMA and 25 Nylon-6 layers as a function of depth (considering depth to be a single step of 250 µm from the PMMA and 25 steps of 100 µm each from the Nylon-6) for the Geant4 and SRIM simulations together with their ratio underneath. Here we can see how the results agree perfectly within the uncertainty of the Geant4 calculation. Furthermore, the exact value does not differ more than 1% for all targets except for the last four, where the difference is still below 4%. Further simulations with different combinations of targets and materials where made obtaining the same results in both simulation codes. Table 3 includes the maximum number of targets that will be used for the real experiment, which were chosen to be the ones given by the simulation minus few targets to be sure that the beam is not stopped.

3.3 Detection set-ups: NaI in coincidence, NaI singles and PET/CT.

When irradiating PE, PMMA and Nylon-6 films with protons of energies up to 18 MeV, the reactions described in the previous section take place, producing ^{11}C and ^{13}N. These isotopes decay by emitting a positron that will eventually annihilate with an electron from the medium producing two 511 keV photons in opposite directions (180º). However, the range of the 1 MeV positrons in air is around 4 m, thus it is necessary to add extra material surrounding the irradiated targets to ensure its annihilation within a small and well defined position.

In order to estimate how thick the converter material needed to be to ensure the positron anihilation, positron emission from inside the irradiated layers was simulated with Geant4. In general, the probability of positron anihilation increases with the atomic number of the element that the material is made of, since the number of electrons of the material also increases with it. Since lead has a high Z and there was plenity of material avaliable, Pb layers of the same size as the target (25mm $\times$ 25mm) placed in front and behind it were the material chosen to be the conversors.

The maximum and average positron emission energies in the β^+ decay of ^{11}C and ^{13}N are 960.5 keV, 385.7 keV, and 1198.45 keV, 493.0 keV respectively. The simulations were performed at all these energies and considering both a punctual and gaussian (a gaussian in XY plane uniform in Z direction) isotropic emission points distribution. As an example, Figure 10 shows the results of 960.5 keV positron anihilation points in the target ($z \in$ [-0.1, 0.1], $x, y \in$ [-12.5, 12.5]) and Pb conversor (0.1$\leq |z| \leq$1.6 and $x, y \in$ [-12.5, 12.5]). This simulation together with other, (considering different energy and emission point distributions), showed that with 0,5 mm of Pb for the z direction and 25 mm $\times$ 25 mm targets are enough for all the positrons to annihilate. Despite 0,5 mm was enough, since the avaliable Pb was 1,5 mm thick, this is the one that was used.

Once the annihilation of positrons is ensured, it is necessary to establish the 511 keV photon detection system. Two types of detectors were proposed: Sodium Iodide scintillators NaI(Tl), and a PET/CT system.

Concerning NaI(Tl), ideally the measurement would be made with the detectors located one in front of the other on both sides of the irradiated targets, and measuring coincidence photons emitted simultaneously in the annihilation. This would eliminate the background in the measurement. However, after some trial measurements had been made, because of the efficiency of this detection system, it was concluded that it would have been required to generate very

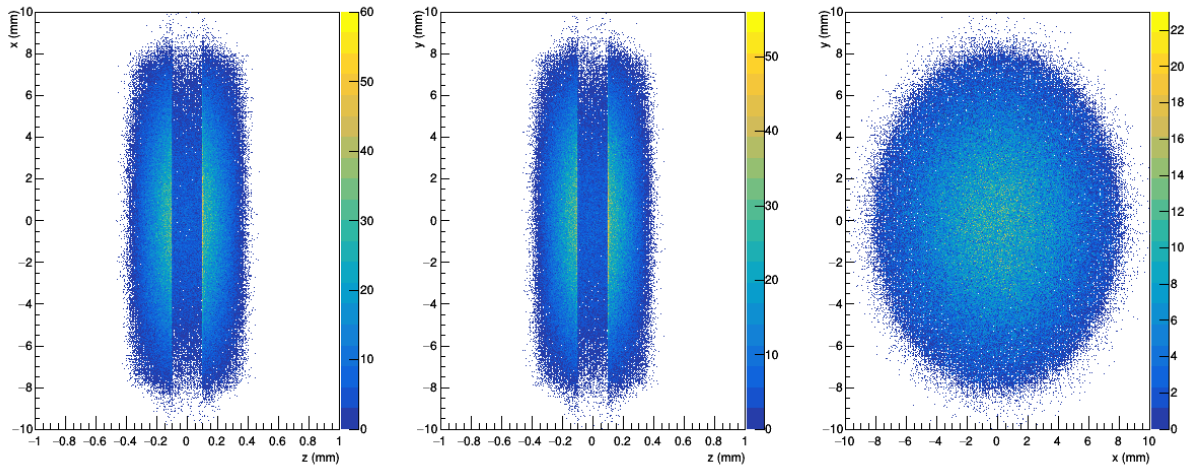

Figure 10: *Geant4 simulation of the annihilation points of 960,5 keV positrons in a 0,2 mm PE target with two 1,5 mm Pb conversors on both sides.*

high activity rates. These are not allowed to be produced due to the radioprotection limits of the facility and therefore, a set of four NaI(Tl) detectors measuring one layer each was chosen instead, and the background was identified and eliminated using data analysis techniques as it will be shown in the next section.

The detectors were placed close to each other with a 10 cm thick Pb bulk between each of them as shielding to avoid cross talk (Figure 7). Each detector consisted of a 2"$\times$ 2" NaI(Tl) scintillator crystal and a photomultiplyer tube. Moreover, three of the detectors had a Canberra 2007P voltage divider which included a preamplifier inside (detectors 1, 3 and 4), while detector 2 had a Canberra 2007 voltage divider without it but with an external preamplifier after it instead. All of the detectors were connected to an up to 2 kV high voltage supply and the detectors which included a 2007P also had connected a 12 V power supply for the preamplifier. The signal was transported through a BNC cable to an amplifier after which it was connected to the CAEN Digitizer Mod. V1720, which output is connected through an optic fiber cable to a PC.

The signal Digitizer Mod. V1720 features 8 channels, 12 bits and 250 MS/s. This digitizer can be adjusted to calculate the baseline of a signal, identify signals above a given threshold, and calculate the area of the signal for the duration chosen, returning to the user the time and integral of each signal.

In addition to the measurements carried out with the NaI(Tl) detectors, another one has

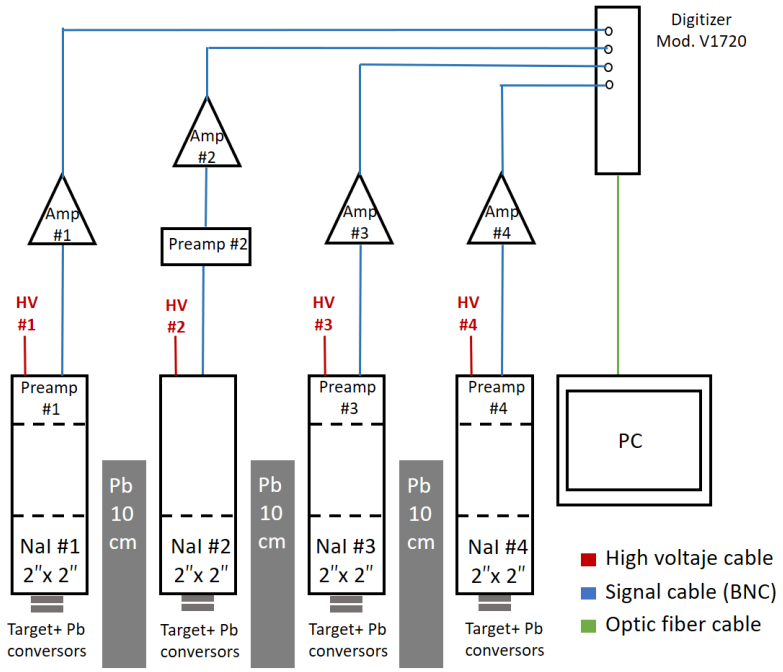

Figure 11: *Scheme of the NaI detection set-up.*

been made with the PET/CT (Siemens PET/CT Biograph mCT-64) avaliable at CNA (Figure 12). The "Positron Emission Tomography" detector consists of an array of 64 Lutetium Oxyorthosilicate (LSO) scintillator detectors displayed forming a ring. These detectors measure 511 keV photons in coincidence emitted inside the ring within a time window of about 4,5 ns.

The CT scan makes use of computer-processed combinations of many X-ray measurements taken from different angles to produce a 3D image of the interior of a person or object that can then be superimposed to the PET image.

The PET detector is normally used for cancer diagnosis by providing the patient with a substance which contains a β^+ emitter isotope and it's likely to be abosorbed by the tumour cells. This isotope will decay emitting positrons that will annihilate producing two 511 keV photons to be detected by the PET. By reconstructing the data taken, the PET detector provides the points over the CT image where the emission of photons, and hence where the cancer might be, is more intense.

In this work, the PET/CT detector has received a different use. This consisted in placing all of the targets inside it and obtaining the total number of counts registered from each target every minute, *i.e.* the activity curve. A more detailed explanation of the reconstruction process and data analysis is provided in the next section.

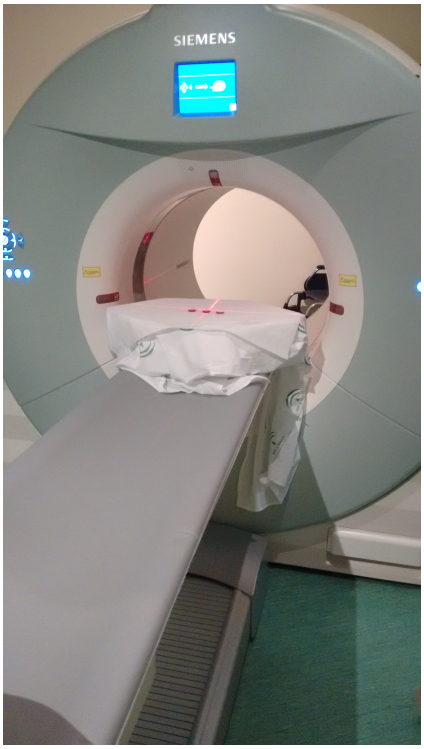

Figure 12: *PET/CT detector at CNA.*

3.4 Characterization of the detection set-up

3.4.1 NaI(Tl) scintillator detector: energy and efficiency calibration

A thallium-doped sodium iodide detector, NaI(Tl), is an inorganic crystal scintillator detector frequently used for gamma spectroscopy. When a photon enters in this crystal, it might interact with the atoms of the crystal mainly by photoelectric effect, Compton scattering or pair production (depending on its energy). The electron/positron pair created in the process, or the electrons which the photon has interacted with, travel within the crystal ionizing the medium. Basically, this ionization consists in the excitation of molecules that after de-excitation emit new photons in the visible spectrum. These photons will be reflected in the walls which contain the crystal until they reach the photocathode, where through photoelectric effect will produce new electrons. Finally, these electrons will be accelerated and multiplied in a certain number of stages in the photomultiplyer tube (PMT) increasing considerably their number. The corresponding current signal is transformed into a pulse of small voltage that is then magnified in the preamplifier and amplifier stages. The voltage of this signal is proportional to the energy that the gamma transfered to the electron in the crystal, thus allowing spectroscopic measurements.

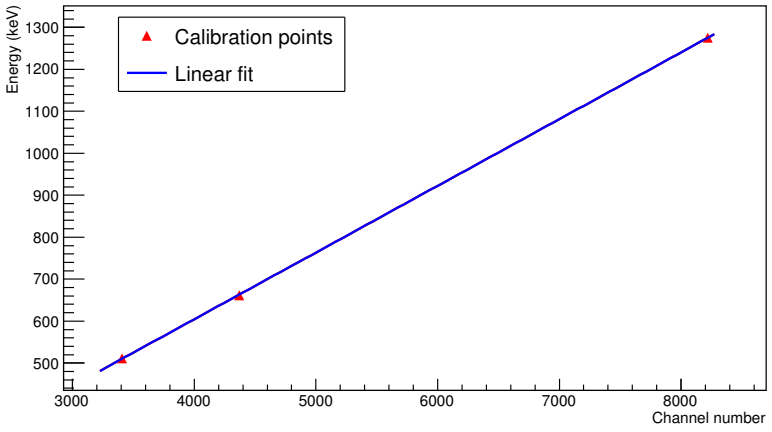

Figure 13: *Example of calibration line for one of the detectors using the 511, 662 and 1275 keV photopeaks from a* ^{137}Cs *and* ^{22}Na *sources.*

In order to measure the activation of the irradiated targets, an energy and efficiency calibration of the four detectors that were used needs to be made. The energy calibration was made with known ^{137}Cs (662 keV) and ^{22}Na (511 and 1275 keV) gamma sources. The channel associated to each of the three photopeaks was estimated as the centroid of the correspoding Gaussian fit. The calibration line is obtained fitting the points to a straigh line in an energy vs. channel scatter plot, as shown Figure 13 in for one of the NaI detectors.

In addition, it is necesary to determine the 511 keV photopeak efficiency of the four detectors so that the number of β^+ emitter nuclei can be calculated from the number of 511 keV photons measured. The probability of a photon depositing all of its energy inside the detector depends on the angle with which the photon enters the detector (*e.g.* a photon that crosses the whole detector is more likely to deposit all of its energy than another one which only crosses a part of it). For this reason, the efficiency calibration can not simply be done with a 511 keV gamma emiter source, since in the irradiation experiment:

a) the 511 keV photons are emitted from the positron annihilation positions and therefore they are not emitted isotropically from a point source but from a distribution in space, and

b) the beam profile is a double gaussian and thus the β^+ emitters produced in the target follow a similar distribution in the XY plane (as it is shown in Figure 10).

As a result, the photopeak efficiency was estimated using both the experimental data and Geant4 to simulate the positron emission, target, Pb conversors and NaI(Tl) detector. First,

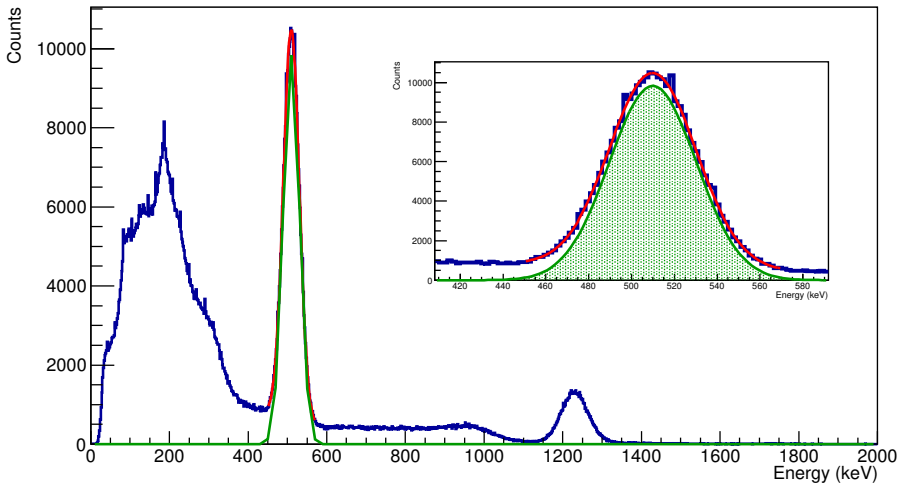

Figure 14: *Graphical illustration of the 511 keV photopeak gaussian plus straight line fit used to calculate the number of counts in it.*

the experimental photopeak efficiency of the detectors was measured using a ^{22}Na source. The measurement was performed with and without two 1,5 mm thick Pb layers at both sides of the target. This efficiency was calculated by dividing the number of counts in the photopeak by the total number of photons emitted (given by the source activity with a 6% uncertainty). The counts in the photopeak were obtained by fitting the peak to a gaussian and a straight line (representing the Compton background) and integrating only the gaussian (see Figure 14). The results for these experimental efficiencies are summarized in the first columns of Table 4, where there is no data for detector 2 because it was not working correctly neither in the calibration nor in the irradiation measurement.

Following on from that, the Geant4 simulations were performed (Figure 15). The geometry of the detector, targets and Pb conversors was implemented using the information provided by the suppliers (detector dimensions, target and detector material densities, etc). Three simulations were performed: two with an isotropical point-like 511 keV photon emission with and without Pb layers (in order to compare and validate with the previous experimental results) and one more with positrons and the Pb conversor (with a gaussian distribution of isotropic emission points), considered the realistic case for the activation experiment.

The results of the simulations showed that, Geant4 overestimates the detector efficiency in the case of 511 keV photons emitted isotropically with Pb conversors by ∼6%. Therefore, the evaluated value for the efficiency was estimated as the result of the simulation in the realistic

	Efficiency					
	Experimental		**Geant4**			**Evaluated**
	511 keV photons (^{22}Na)		511 keV photons		Positrons	Positrons
Emission	Point-like	Point-like	Point-like	Point-like	Gaussian	Gaussian
Pb	No	Yes	No	Yes	Yes	Yes
Det. 1	$20{,}0 \pm 1{,}2\%$	$12{,}2 \pm 0{,}7\%$	19,04%	12,91%	16,42%	$15,5 \pm 0{,}9\%$
Det. 2	-	-	-	-	-	-
Det. 3	$19{,}6 \pm 1{,}2\%$	$12{,}1 \pm 0{,}7\%$	19,04%	12,91%	16,42%	$15{,}4 \pm 0{,}9\%$
Det. 4	$20{,}4 \pm 1{,}2\%$	$12{,}1 \pm 0{,}7\%$	19,04%	12,91%	16,42%	$15{,}4 \pm 0{,}9\%$

Table 4: *Experimental and Geant4 simulation results for the efficiency of the different detectors. The statistical uncertainty for the experimental measurements was negligible compared to the systematic uncertainty, 6% coming from the source activity uncertainty. The simulations were made with a large number of events so that the statistical uncertainty was negligible as well. See text for details about the "Evaluated" values.*

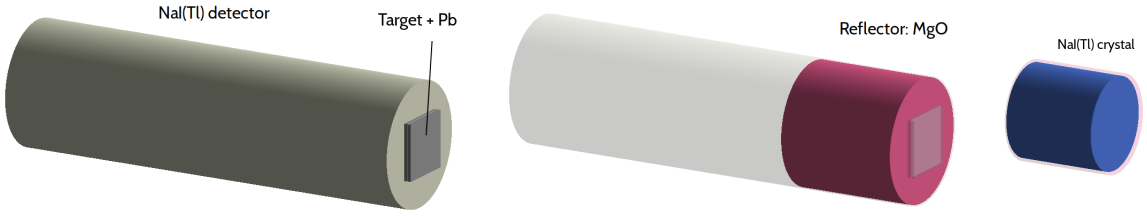

Figure 15: *Detector, targets and Pb conversors implemented in the Geant4 simulation.*

case corrected by this overestimation. The simulations were performed with different positron energies and did not show a significant influence on the efficiency.

3.4.2 PET/CT: reconstruction protocol and efficiency calibration

The main advantage of using the PET/CT detector for the measurement of the activity of the irradiated targets as a function of the time, is its good spatial resolution, which allows measuring all the targets at the same time. On the other hand, the NaI allows measuring only one target per detector at a time.

The PET/CT detector uses a certain reconstruction protocol to find the number of 511 keV photons emitted from a selected region of space at a certain period of time. In this way, one can programme the detector to get the activity that came from aspecific region. However, the raw

Source	Activity (kBq)	PROPCPS	Ratio (Bq/PROPCPS)
^{22}Na - 1	890 ± 60	34208	$26,0 \pm 1,8$
^{22}Na - 2	141 ± 9	6396	$22,0 \pm 1,4$

Table 5: *Activities and PROPCPS of the sources used in the experiment.*

data, *i.e.* the number of counts, is not accessible on these devices. What can be obtained is a characteristic magnitude of these detectors denominated "PROPCPS" (proportional to counts per second), therefore a calibration of the detector is needed.

For this reason, two ^{22}Na samples of known activities were introduced together with the irradiated targets during the measurement. By a simple rule of proportionality, the conversion of PROPCPS to accounts per second can me performed (Table 5). The results show that there is a 15% difference in the efficiency (ratio Bq/propcps) obtained from each source. This difference is larger than the 6% uncertainty of the activity of the sources, and is most probably related to a dependece of the attenuation of gammas inside the PET with the position. This is normally corrected for automatically by the PET image reconstruction protocol; but the system is not prepared to consider the thin layers of lead (high density and high atomic number) used as conversors. Therefore a 15% uncertainty is assumed for the PET detection efficiency.

4 Experiments at CNA with 18 MeV protons

4.1 Irradiation experiments

A total of seven irradiations were performed in this work at the cyclotron external beam line (Figure 16), out of which four were to be measured with the NaI(Tl) detectors and three with the PET/CT scanner.

Figure 16: *Irradiation experiment at the cyclotron external beam line.*

Firstly, the activation of the PE targets to be measured with the NaI detectors was performed, and therefore, since only four detectors were available, four irradiations were required to measure the activity of the thirteen PE films. Detector 1 always measured the activity of the PE-1 in order to use it as a reference and compare the results between irradiations. Table 6 includes the total charge in each irradiation, its duration, the time between the end of the irradiation and the start of the measurement (time offset), and the films that were measured in each detector. The layer number stands for the position of the layer in each irradiation, *e.g.* in the third irradiation 10 PE layers were irradiated but only the first (PE-1), eighth (PE-8), nineth (PE-9) and tenth (PE-10) were measured.

A direct measurement of the ion beam current impinging on the electrically isolated graphite beam dump was carried out using a Brookhaven 1000c Current Integrator. The total fluence is calculated by taking into consideration the secondary electron losses in graphite (previously measured by biasing a graphite target into a vacuum chamber).

The targets from the last three irradiations were measured all at the same time in the PET/CT scanner. For this purpose, they were placed inside the PET/CT detector 1 cm away

from each other with the Pb conversor on top and below and then, they were put inside the PET/CT detector (Figure 17). The irradiated targets were the ones discussed in section 3.2 plus an extra first PE target in order to compare the results from each irradiation. Table 7 contains this information together with the total charge, irradiation and measurement duration, and time offset.

Irradiation	1	2	3	4
Total charge (nC)	3754	4558	5748	4506
Irrad. time	3'	3'	3'	3'
Time offset	19' 40"	21' 4"	20' 44"	23' 5"
Meas. time	3h	2,5h	2,5h	10h
Detector 1	PE-1	PE-1	PE-1	PE-1
Detector 2*	PE-2	PE-5	PE-8	PE-11
Detector 3	PE-3	PE-6	PE-9	PE-12
Detector 4	PE-4	PE-7	PE-10	PE-13

* The detector did not work properly and no data could be extracted from it.

Table 6: *Target irradiation configuration for the measurement with the NaI(Tl) detectors.*

Figure 17: *Irradiated targets display for the measurement with the PET/CT scaenner.*

Irradiation	5	6	7
Total charge (nC)	4479	4060	4525
Irrad. time	3'	3'	3'
Meas. time	3h	3h	3h
Time offset	17' 18"	43' 48"	29' 48"
Targets	PE + 20 Nylon-6	PE + 8 PMMA	13 PE

Table 7: *Target irradiation configuration for the measurement with the PET/CT detector.*

4.2 Data analysis: obtention of the activity curve

The objective of this step of the analysis is to obtain the activity as a function of time and per unit of irradiated charge in each irradiated target from the data provided by the NaI(Tl) and the PET/CT detectors.

As it was mentioned in section 3.3, in the measurements made with the NaI detectors, the Digitizer Mod. V1720 was the device used for the data adquisition. This device provides a list mode file containing the signal integral and the time at which each signal arrived, that is to say that one file containing this information was created in each measurment for each detector. Once the detectors are calibrated in energy and efficiency, to obtain the activity curve one can simply fill a histogram with the number of 511 keV counts per unit time and scale it by the efficiency and charge of the irradiation (for this work a one minute bin width was considered). However, there are background counts below the 511 keV peak. In order to identify and eliminate this background, an energy histogram was filled for every minute and a fit to the photopeak (gaussian plus straight line) was made. The total number of counts in the gaussian part of the fit was filled to each bin of the time histogram. In addition, the time histogram was shifted in time by the time offset of each measurement so that all histograms start at the time of the irradiation. Figure 18 shows this spectrum for the PE-1 target after the first irradiation at the first (left) and last minute of the measurement (right). Furthermore, Figure 19 illustrates the activity per nC obtained with and without eliminating the background below the 511 keV peak and already corrected by each detectors efficiency. All this data analysis was performed with the software ROOT [32] .

The case of the raw data obtained with the PET/CT is rather simpler since it already provides the number of PROPCPS per minute per target. Knowing the total charge of each

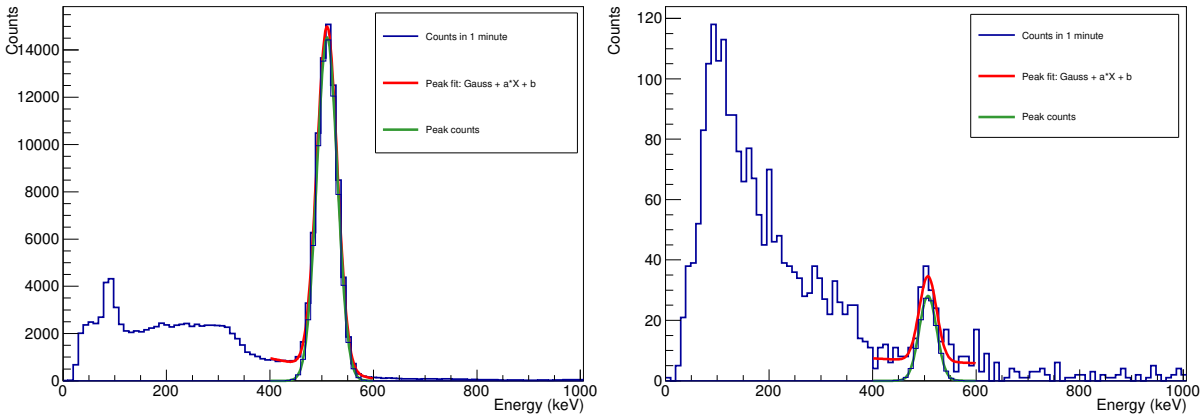

Figure 18: *Example of a photopeak fit for the first minute and last minute spectrum for the target PE-1 after the first irradiation.*

irradiation, the time offset and the conversion factor from PROPCPS to counts (see section 3.4.2) one can scale the raw data curve and obtain the activity per nC.

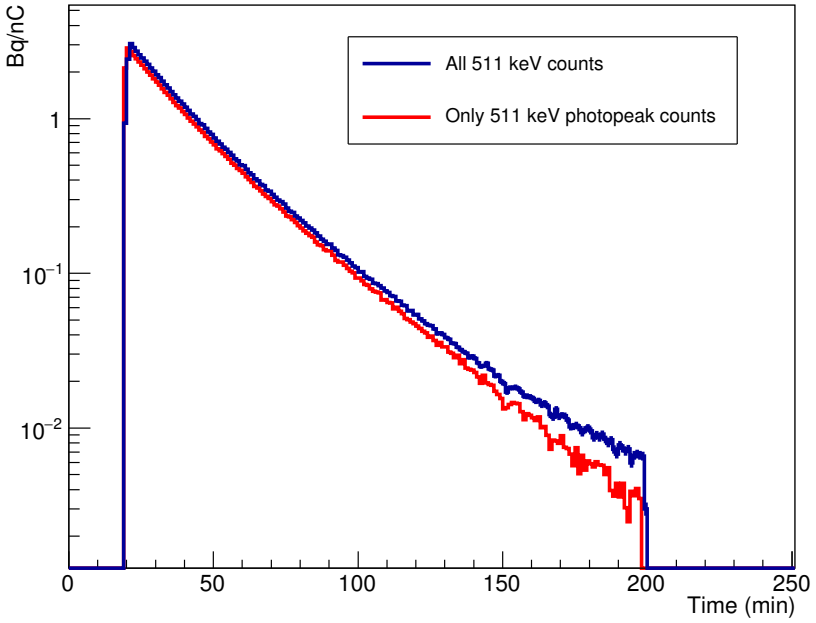

Figure 19: *Activity per nC in the PE-1 target after the first irradiation.*

As it will be shown later, the curves from the PET/CT detector have a background that comes from the ^{177}Lu present in the Lutetium Oxyorthosilicate (LSO) scintillator crystals (2,5% of natural Lutetium). This isotope has a half-life of $3{,}78 \times 10^{10}$ years, hence the background can be considered as a constant (Figure 20). Unfortuntely, this was observed after the measurements

and was not considered in the planing, thus the measurements were taken for "only" 180 minutes. This is not long enough to reach the time at which this constant background dominates. For this reason the background level could not be measured exactly and had to be estimated from fits, as shown in the next section.

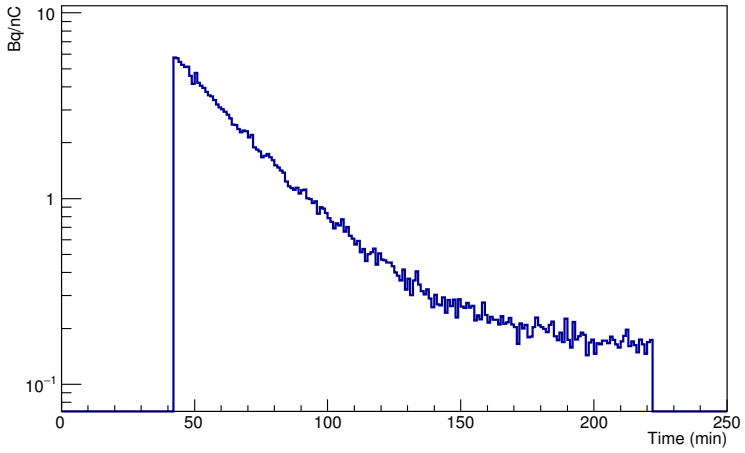

Figure 20: *Activity per nC in a Nylon-6 target placed in front of the beam in the 15^{th} position.*

4.3 Data analysis: from activity curve to production yield and cross section

Once all the activity curves are obtained, the inicial activity or activity produced in the irradiation per nC associated to each PET isotope (^{11}C and ^{13}N) can be calculated. For this purpose, the curves are fitted to two exponential functions (due to the radioactive decay law) plus a constant (only for the PET/CT targets), *i.e.*

$$f(t) = A_0 + A_{11\mathrm{C}} \cdot \exp\left(-\frac{\ln 2}{T_{1/2}^{11\mathrm{C}}}t\right) + A_{13\mathrm{N}} \cdot \exp\left(-\frac{\ln 2}{T_{1/2}^{13\mathrm{N}}}t\right), \tag{4.1}$$

where $A_{11\mathrm{C}}$, $T_{1/2}^{11\mathrm{C}}$, and $A_{13\mathrm{N}}$, $T_{1/2}^{13\mathrm{N}}$ are the initial activities per nC and half-lifes for ^{11}C and ^{13}N respectively. The fit was performed fixing the half-lifes to 20,361 min and 9,967 min and leaving A_0, $A_{11\mathrm{C}}$ and $A_{13\mathrm{N}}$ as free parameters. The fit was done making use of the ROOT software framework whose algorithms are based on the minimum chi-squared method. Figure 21 shows an example of the fits results for a PE target (left) and a Nylon-6 (right) one.

Tables 8, 9 and 10 contain the fit results for each irradiated target and their uncertainty. The different sources of systematic uncertainty in the measurement of the initial activities were: the uncertainty in the detector efficiency ($\varepsilon_e = 6\%$ for the NaI detectors and $\varepsilon_e = 15\%$ for the PET/CT scanner), the uncertainty in the measurement of the proton current (estimated to be $\varepsilon_c = 5\%$) and the uncertainty in the curve fit (ε_f). The latter is variable, *i.e.* it depends on each target. ROOT provides the uncertainty in the fit parameters, but these has been found

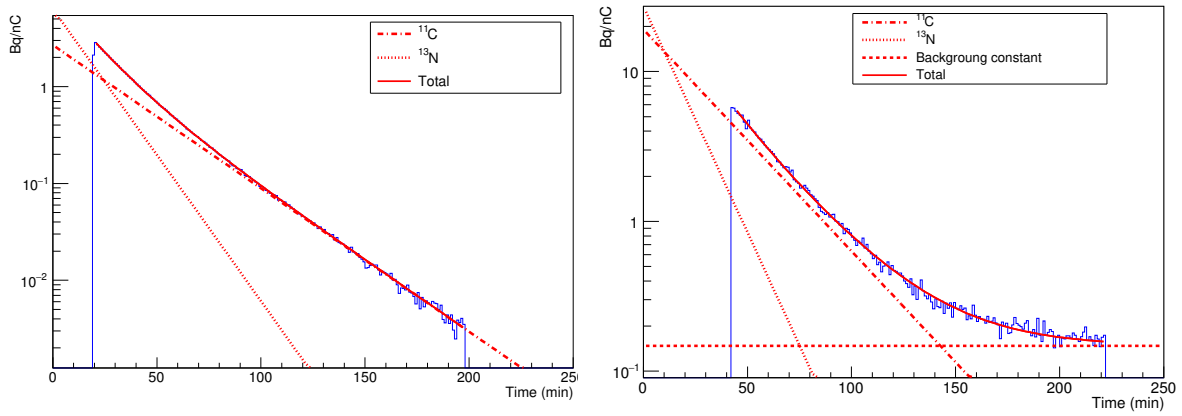

Figure 21: *PE-1 (left) and Nylon6-15 (right) target activation curve fit. The first one measured with the NaI detectors and the latter in the PET/CT.*

to be unrealistically small, especially when the sample activity is low and the background has to be fitted as well (targets measured with the PET/CT system). The realistic uncertainties were estimated by fixing some of the parameters (one at a time) within small variations of the optimum value (given by ROOT's fit) and finding out wether if the fit is still good. Once this uncertainty is calculated, the total relative uncertainty is given by

$$\varepsilon = \sqrt{\varepsilon_e^2 + \varepsilon_c^2 + \varepsilon_f^2} \tag{4.2}$$

Energy (MeV)	^{13}N (Bq/nC)	^{11}C (Bq/nC)
$17{,}0^{+0{,}4}_{-0{,}4}$	$6{,}4 \pm 1{,}3$	$2{,}69 \pm 0{,}4$
$16{,}4^{+0{,}5}_{-0{,}5}$	$3{,}5 \pm 0{,}7$	$0{,}03 \pm 0{,}03$
$15{,}8^{+0{,}5}_{-0{,}5}$	$3{,}1 \pm 0{,}5$	$0{,}012 \pm 0{,}012$
$15{,}2^{+0{,}5}_{-0{,}5}$	$3{,}3 \pm 0{,}5$	$0{,}072 \pm 0{,}021$
$13{,}8^{+0{,}6}_{-0{,}6}$	$3{,}7 \pm 0{,}6$	$0{,}108 \pm 0{,}024$
$11{,}5^{+0{,}7}_{-0{,}7}$	$3{,}2 \pm 0{,}5$	$0{,}057 \pm 0{,}012$
$10{,}6^{+0{,}7}_{-0{,}7}$	$4{,}4 \pm 0{,}7$	$0{,}22 \pm 0{,}05$
$8{,}7^{+0{,}8}_{-0{,}9}$	$7{,}0 \pm 1{,}2$	$0{,}03 \pm 0{,}03$
$8^{+0{,}9}_{-1}$	$9{,}6 \pm 1{,}6$	$0{,}26 \pm 0{,}06$

Table 8: *Activity per Bq produced in each PE target, thus as function of the proton energy. These data were taken with the NaI detectors since the data taken from the PE targets measured with the PET/CT had a low activity rate and no trustful data could be extracted from the measurement.*

Energy (MeV)	^{13}N (Bq/nC)	^{11}C (Bq/nC)
$16{,}3^{+0,6}_{-0,6}$	37 ± 7	$0{,}4 \pm 0{,}4$
$15{,}4^{+0,6}_{-0,7}$	75 ± 14	-*
$14{,}4^{+0,7}_{-0,7}$	116 ± 22	-*
$13{,}4^{+0,7}_{-0,8}$	86 ± 16	$0{,}5 \pm 0{,}5$
$12{,}3^{+0,8}_{-0,8}$	98 ± 18	$0{,}5 \pm 0{,}5$
$11{,}1^{+0,9}_{-0,9}$	143 ± 27	$0{,}6 \pm 0{,}6$
$9{,}8^{+1,0}_{-1,0}$	95 ± 18	$0{,}4 \pm 0{,}4$
$8{,}3^{+1,1}_{-1,2}$	72 ± 13	$1{,}3 \pm 0{,}6$

* The results of these fits could not be trusted because of the low activity of the ^{11}C, which made it imposible to distinguish it from the background

Table 9: *Activity per nC produced in each PMMA target, thus as function of the proton energy.*

Energy (MeV)	^{13}N (Bq/nC)	Act. ^{11}C (Bq/nC)
$16{,}6^{+0,3}_{-0,3}$	29 ± 9	$10{,}3 \pm 1{,}9$
$16{,}2^{+0,3}_{-0,3}$	28 ± 5	$10{,}3 \pm 2{,}1$
$15{,}9^{+0,3}_{-0,4}$	23 ± 4	$9{,}2 \pm 1{,}8$
$15{,}5^{+0,4}_{-0,4}$	27 ± 8	$12{,}1 \pm 2{,}3$
$15{,}1^{+0,4}_{-0,4}$	36 ± 11	$12{,}1 \pm 2{,}3$
$14{,}7^{+0,4}_{-0,4}$	14 ± 3	$3{,}7 \pm 0{,}7$
$14{,}4^{+0,4}_{-0,4}$	38 ± 7	14 ± 3
$14{,}0^{+0,4}_{-0,4}$	43 ± 8	14 ± 3
$13{,}6^{-0,4}_{-0,4}$	37 ± 7	13 ± 3
$13{,}1^{+0,4}_{-0,4}$	37 ± 7	14 ± 3
$12{,}7^{+0,4}_{-0,4}$	33 ± 10	20 ± 4
$12{,}3^{-0,5}_{-0,5}$	40 ± 12	21 ± 4
$11{,}8^{+0,5}_{-0,5}$	33 ± 10	20 ± 4
$11{,}4^{+0,5}_{-0,5}$	28 ± 5	19 ± 4
$10{,}9^{+0,5}_{-0,5}$	27 ± 5	19 ± 4
$10{,}4^{+0,5}_{-0,6}$	23 ± 4	17 ± 3
$9{,}8^{+0,6}_{-0,6}$	26 ± 8	16 ± 3
$8{,}1^{+0,7}_{-0,7}$	41 ± 8	19 ± 4

Table 10: *Activity per nC produced in each Nylon-6 target, thus as function of the proton energy.*

k \ j	H (at/cm^2)	C (at/cm^2)	N (at/cm^2)	O (at/cm^2)
PE	$1{,}62 \cdot 10^{21}$	$8{,}09 \cdot 10^{20}$	0	0
PMMA	$1{,}43 \cdot 10^{21}$	$8{,}96 \cdot 10^{20}$	0	$3{,}58 \cdot 10^{20}$
Nylon-6	$6{,}62 \cdot 10^{20}$	$3{,}61 \cdot 10^{20}$	$6{,}02 \cdot 10^{19}$	$6{,}02 \cdot 10^{19}$

Table 11: *Number of atoms per cm^2 of each element in each target.*

Knowing the initial activity per nC, the production yield of the isotope i, produced in a proton induced reaction in the isotope j measured in the target k is given by

$$Y^k_{j\to i} = \frac{A^k_i \cdot |e|}{\lambda_i} = \frac{A^k_i \cdot |e| \cdot T^i_{1/2}}{\ln 2} \tag{4.3}$$

where e is the charge of the electron, λ_i is the exponential decay constant, A^k_i is the initial activity per nC associated to the produced isotope i (^{11}C or ^{13}N) in the target k (PE, PMMA or Nylon-6) and $T^i_{1/2}$ is its half-life. The production yield in each target is, on the other hand, related to the different cross sections involved. For instance, the total production yield of the isotope i in the target k, since ^{11}C and ^{13}N can not be produced with H, is

$$Y^k_i = \sum_j n^k_j p_j \sigma_{j\to i} = n^k_{\mathrm{C}} \cdot p_{\mathrm{C}} \cdot \sigma_{C\to i} + n^k_{\mathrm{O}} \cdot p_{\mathrm{O}} \cdot \sigma_{O\to i} + n^k_{\mathrm{N}} \cdot p_{\mathrm{N}} \cdot \sigma_{N\to i}, \tag{4.4}$$

where C, O and N stand for $^{\mathrm{nat}}$C, $^{\mathrm{nat}}$O and $^{\mathrm{nat}}$N respectively and their presence depends on the target material, p_j is the isotopic natural abundance of the target isotope or element j ($p_{\mathrm{C}} = p_{12\mathrm{C}} + p_{13\mathrm{C}}$, $p_{\mathrm{O}} \simeq p_{16\mathrm{O}}$ and $p_{\mathrm{N}} \simeq p_{14\mathrm{N}}$) and n^k_j is the number of atoms per barn of the element j in the target k, which can be calculated from the material's density and is included in Table 11.

The ^{11}C and ^{13}N production cross sections can be obtained for each material by using equation 4.3 and 4.4 together with the data from Table 11 and the isotopic abundances ($^{\mathrm{nat}}$C= 98,9% ^{12}C+ 1,1% ^{13}C; $^{\mathrm{nat}}$O$\simeq$ 99,8% ^{16}O; $^{\mathrm{nat}}$N $\simeq$ 99,6% ^{14}N). However, since PMMA and Nylon-6 contain different elements, and therefore different reaction channels that contribute to the production of ^{11}C and ^{13}N, the contribution of each reaction channel can't be distinguished with the measurement of only one material. On the other hand, in PE only $^{\mathrm{nat}}$C contributes to the production cross section of ^{11}C and ^{13}N, then

$$Y^{\mathrm{PE}}_i = Y^{\mathrm{PE}}_{\mathrm{C}\to i} = n^{\mathrm{PE}}_{12\mathrm{C}} \cdot p_{12\mathrm{C}} \cdot \sigma_{12\mathrm{C}\to i} + n^{\mathrm{PE}}_{12\mathrm{C}} \cdot p_{13\mathrm{C}} \cdot \sigma_{13\mathrm{C}\to i} = n^{\mathrm{PE}}_{\mathrm{C}} \cdot \sigma_{\mathrm{C}\to i}, \tag{4.5}$$

and

$$\sigma_{\mathrm{C}\to i} = \frac{Y_{\mathrm{C}}^{\mathrm{PE}}}{n_{\mathrm{C}}^{\mathrm{PE}}} = \frac{A_i^{\mathrm{PE}} \cdot |e| \cdot T_{1/2}^i}{\ln 2 \cdot n_{\mathrm{C}}^{\mathrm{PE}}}, \tag{4.6}$$

where i stands again for the produced isotope (^{11}C or ^{13}N) and A_i^{PE} is the activity produced per nC of the isotope i in PE. These production cross sections in $^{\mathrm{nat}}$C, ($\sigma_{\mathrm{C}\to 11C}$ and $\sigma_{\mathrm{C}\to 13N}$), can be substracted from the ones in PMMA in order to obtain the production cross sections in $^{\mathrm{nat}}$O,

$$Y_i^{\mathrm{PMMA}} = \frac{A_i^{\mathrm{PMMA}} \cdot |e| \cdot T_{1/2}^i}{\ln 2} = Y_{\mathrm{C}\to i}^{\mathrm{PMMA}} + Y_{\mathrm{O}\to i}^{\mathrm{PMMA}} = n_{\mathrm{C}}^{\mathrm{PMMA}} \cdot \sigma_{C\to i} + n_{\mathrm{O}}^{\mathrm{PMMA}} \cdot p_{16\mathrm{O}} \cdot \sigma_{16O\to i} \tag{4.7}$$

$$\sigma_{16\mathrm{O}\to i} = \frac{A_i^{\mathrm{PMMA}} \cdot |e| \cdot T_{1/2}^i}{\ln 2 \cdot n_{\mathrm{O}}^{\mathrm{PMMA}} \cdot p_{16\mathrm{O}}} - \frac{n_{\mathrm{C}}^{\mathrm{PMMA}}}{p_{16\mathrm{O}} \cdot n_{\mathrm{O}}^{\mathrm{PMMA}}} \sigma_{\mathrm{C}\to i}, \tag{4.8}$$

and similarly, for the Nylon-6 targets, we can also obtain the production cross sections,

$$\sigma_{14\mathrm{N}\to i} = \frac{Y_i^{\mathrm{Nylon}} - n_{\mathrm{O}}^{\mathrm{Nylon}} \cdot \sigma_{16\mathrm{O}\to i} - n_{\mathrm{C}}^{\mathrm{Nylon}} \cdot \sigma_{\mathrm{C}\to i}}{p_{14\mathrm{N}} \cdot n_{\mathrm{N}}^{\mathrm{Nylon}}}, \tag{4.9}$$

where

$$Y_i^{\mathrm{Nylon}} = \frac{A_i^{\mathrm{Nylon}} \cdot |e| \cdot T_{1/2}^i}{\ln 2} \tag{4.10}$$

Due to the fact that the production cross sections $^{\mathrm{nat}}$O(p, *) and $^{\mathrm{nat}}$N(p, *) are computed by subtracting $^{\mathrm{nat}}$C(p, *), and $^{\mathrm{nat}}$C(p, *) and $^{\mathrm{nat}}$O(p,*), respectively, this introduces a certain correlation between them. The quantification of this correlation has not been estimated yet and will be tackled in the future. Furthermore, the energies at which each yield was measured are different, since different targets and thicknesses were used. As a result, the substraction of the measured production cross sections is not possible without performing an interpolation of the data. Figure 22 shows a representation of the ^{11}C and ^{13}N production yields in all of the irradiated targets together with the interpolated energy points, which are the same energy points for every target. The errors in the measured yield points were obtained by uncertainty propagation of the ones from the initial activities, while the error in the interpolated yields was matched to the nearest measured point. Regarding the energy uncertainty, it has been chosen (based on the experimental values) to decrease linearly from 1 MeV at 8 MeV to 0.5 MeV at 17 MeV.

Finally, the production cross sections were calculated using equations 4.6, 4.8 and 4.9, resulting in the values shown in Tables 12 and 13 contain these results. Once again, the errors were properly propagated. The large uncertainty in some of the cross section values is due to the previously mentioned large error in the fit plus the error propagation in the substraction of the production yields. Figure 23 illustrates these results.

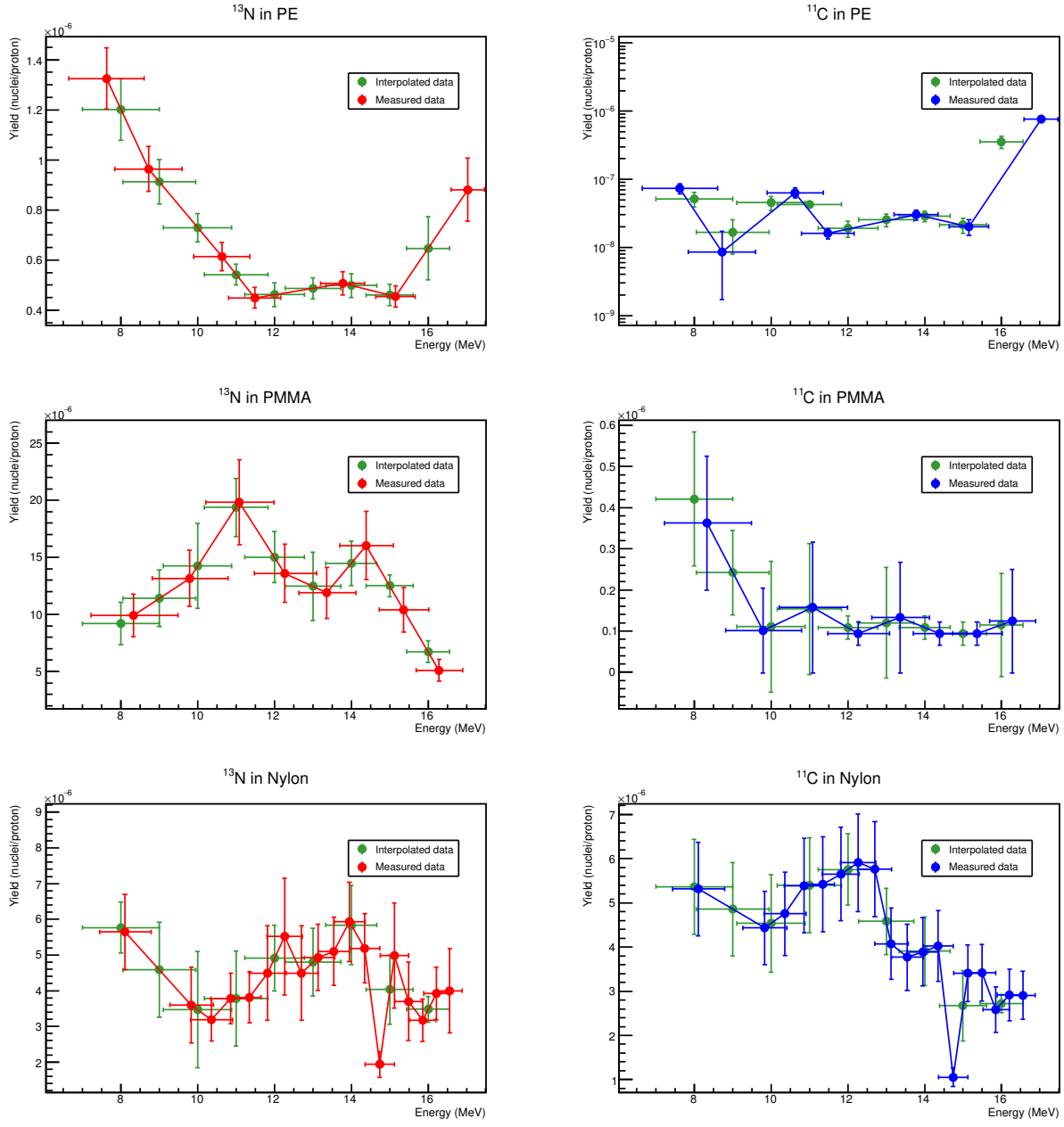

Figure 22: *Measured and interpolated ^{11}C and ^{13}N production yields in PE, PMMA and Nylon-6.*

Energy (MeV)	^{nat}C(p,*)^{11}C (mb)	^{nat}O(p,*)^{11}C (mb)	^{nat}N(p,*)^{11}C (mb)
8 ± 1	$0{,}063 \pm 0{,}015$	$1{,}0 \pm 0{,}5$	88 ± 18
$9{,}0 \pm 0{,}9$	$0{,}021 \pm 0{,}011$	$0{,}6 \pm 0{,}3$	80 ± 18
$10{,}0 \pm 0{,}9$	$0{,}056 \pm 0{,}013$	$0{,}2 \pm 0{,}5$	75 ± 19
$11{,}0 \pm 0{,}8$	$0{,}053 \pm 0{,}003$	$0{,}3 \pm 0{,}5$	89 ± 18
$12{,}0 \pm 0{,}8$	$0{,}024 \pm 0{,}006$	$0{,}24 \pm 0{,}09$	95 ± 14
$13{,}0 \pm 0{,}7$	$0{,}032 \pm 0{,}007$	$0{,}3 \pm 0{,}4$	76 ± 13
$14{,}0 \pm 0{,}7$	$0{,}036 \pm 0{,}006$	$0{,}22 \pm 0{,}09$	64 ± 13
$15{,}0 \pm 0{,}6$	$0{,}026 \pm 0{,}007$	$0{,}20 \pm 0{,}10$	44 ± 13
$16{,}0 \pm 0{,}6$	$0{,}438 \pm 0{,}09$		43 ± 5

Table 12: *Measured production cross section of ^{11}C in ^{nat}C, ^{nat}O and ^{nat}N.*

Energy (MeV)	^{nat}C(p,*)^{11}C (mb)	^{nat}O(p,*)^{11}C (mb)	^{nat}N(p,*)^{11}C (mb)
8 ± 1	$1{,}49 \pm 0{,}15$	22 ± 6	65 ± 18
$9{,}0 \pm 0{,}9$	$1{,}13 \pm 0{,}11$	29 ± 7	40 ± 30
$10{,}0 \pm 0{,}9$	$0{,}90 \pm 0{,}07$	38 ± 11	15 ± 38
$11{,}0 \pm 0{,}8$	$0{,}67 \pm 0{,}05$	52 ± 7	6 ± 30
$12{,}0 \pm 0{,}8$	$0{,}57 \pm 0{,}06$	41 ± 6	38 ± 22
$13{,}0 \pm 0{,}7$	$0{,}60 \pm 0{,}05$	33 ± 9	43 ± 25
$14{,}0 \pm 0{,}7$	$0{,}62 \pm 0{,}06$	39 ± 6	54 ± 24
$15{,}0 \pm 0{,}6$	$0{,}57 \pm 0{,}05$	34 ± 3	30 ± 19
$16{,}0 \pm 0{,}6$	$0{,}80 \pm 0{,}16$	17 ± 3	36 ± 10

Table 13: *Measured production cross section of N^{13} in ^{nat}C, ^{nat}O and ^{nat}N.*

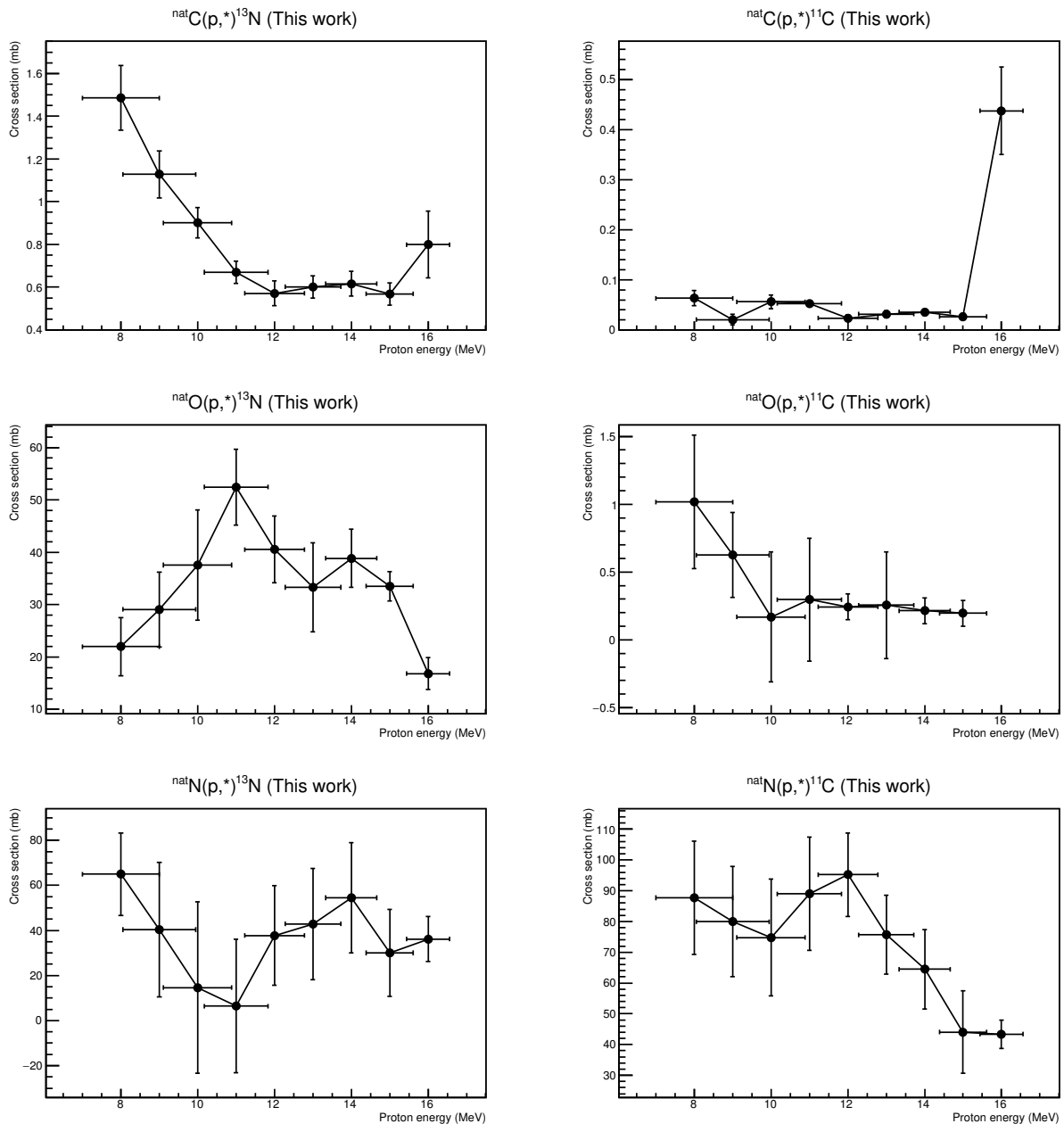

Figure 23: *Production cross sections of* ^{11}C *and* ^{13}N *in* ^{nat}C, ^{nat}O *and* ^{nat}N *measured in this work.*

4.4 Comparison to other experimental data and discussion

After obtaining the production cross sections of ^{11}C and ^{13}N for ^{nat}C, ^{nat}O and ^{nat}N, a comparison with the cross sections avaliable in the EXFOR database has been performed. Unfortunatelly, the cross section in ^{nat}C can not be compared directly with the^{12}C(p,*) and ^{13}C(p,*) reactions avaliable in EXFOR, since in the data measured in this work is not possible to distinguish between the contribution from these two isotopes to the different reaction channels. However, there is one measurement provided by [33] in ^{nat}C. Figure 24 shows the avaliable data in EXFOR for the ^{nat}C(p,*)^{11}C, ^{12}C(p,pn)^{11}C and ^{13}C(p,p2n)^{11}C reactions cross sections together with the data obtained in this work. It looks clear that our data are below all previous measurements. However, it is also observed that there is a large disagreement among the data aviable, with differences of a factor of 50 between different data sets around 18 MeV.

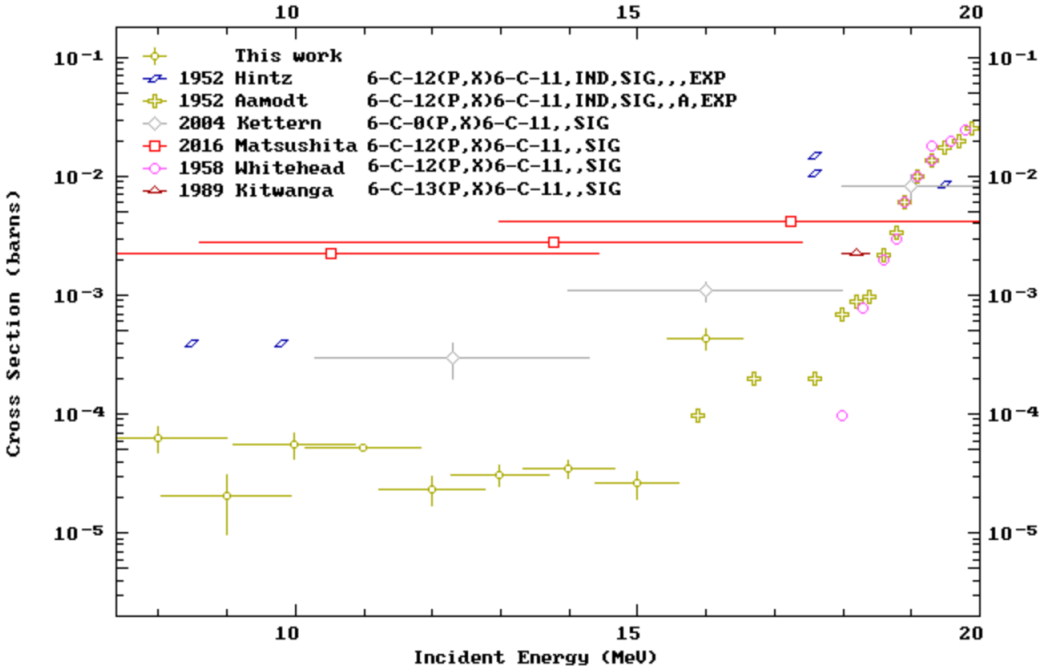

Figure 24: *^{nat}C(p,*)^{11}C, ^{12}C(p,pn)^{11}C and ^{13}C(p,p2n)^{11}C cross section data avaliable in the EXFOR database together with the ^{nat}C(p,*)^{11}C measured in this work.*

In contrast, the production cross sections in ^{nat}O and ^{nat}N are directly comparable with the reaction channels ^{16}O(p,*) and ^{14}N(p,*). Figures 25 and 26 represent the results obtained in this work together with all the data in the energy range of interest and available at EXFOR. It is clear that the reactions ^{16}O(p,*)^{13}N and ^{14}N(p,*)^{11}C have been extensively measured. Indeed, except at high energy in the ^{14}N(p,*)^{11}C reaction, our data are in agreement within uncertainties

with the majority of the available data.

Regarding the production of ^{11}C via ^{16}O(p,*) and production of ^{13}N via ^{14}N(p,*), there are not as many measurements. For the ^{16}O(p,*)^{11}C reaction there are only two points measured in the range at 7 and 19 MeV. Our results, with a sizable uncertainty dominated by the fits of the curve activtes in PMMA for the production of ^{11}C , are in agreement with the data available at low energy ($\sim$7 MeV), while at $\sim$19 MeV they can not be directly compared because the maximum energy of our data for this reaction is 16 MeV.

On the other hand, the ^{14}N(p,*)^{13}N has recently been measured by K. Kovacs [25] in the range from 11 to 18 MeV, with results that are around a factor of two higher than the previous data by Sajjad. Besides, in this energy range (11-18 MeV) our results are significantly above (between of factor of 1 to 4) the previous data, while at below 11 MeV ours are the first data available.

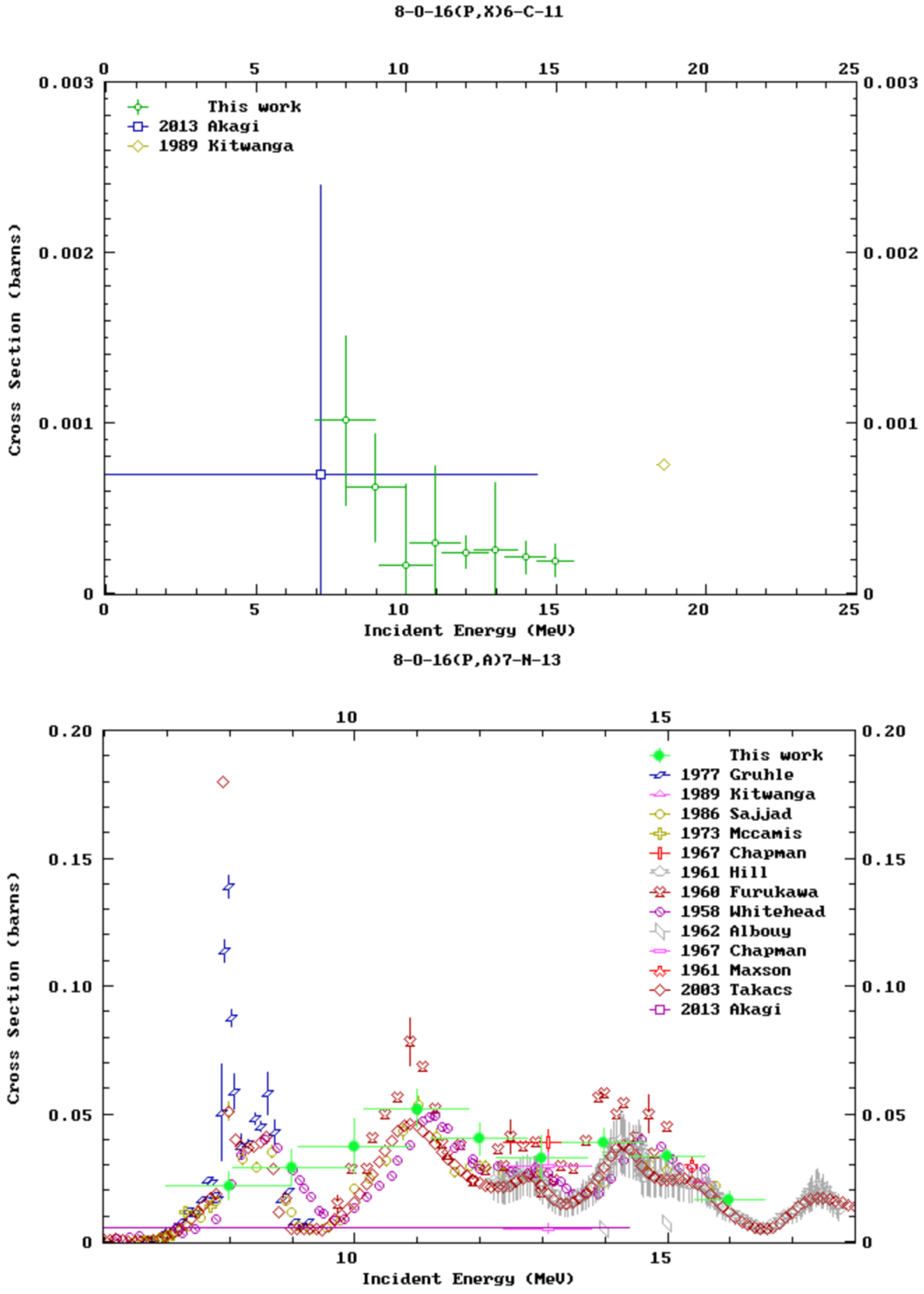

Figure 25: *$^{16}O(p,*)^{11}C$ and $^{16}O(p,*)^{13}N$ cross section comparison between measured data in this work and previous experimental results from EXFOR.*

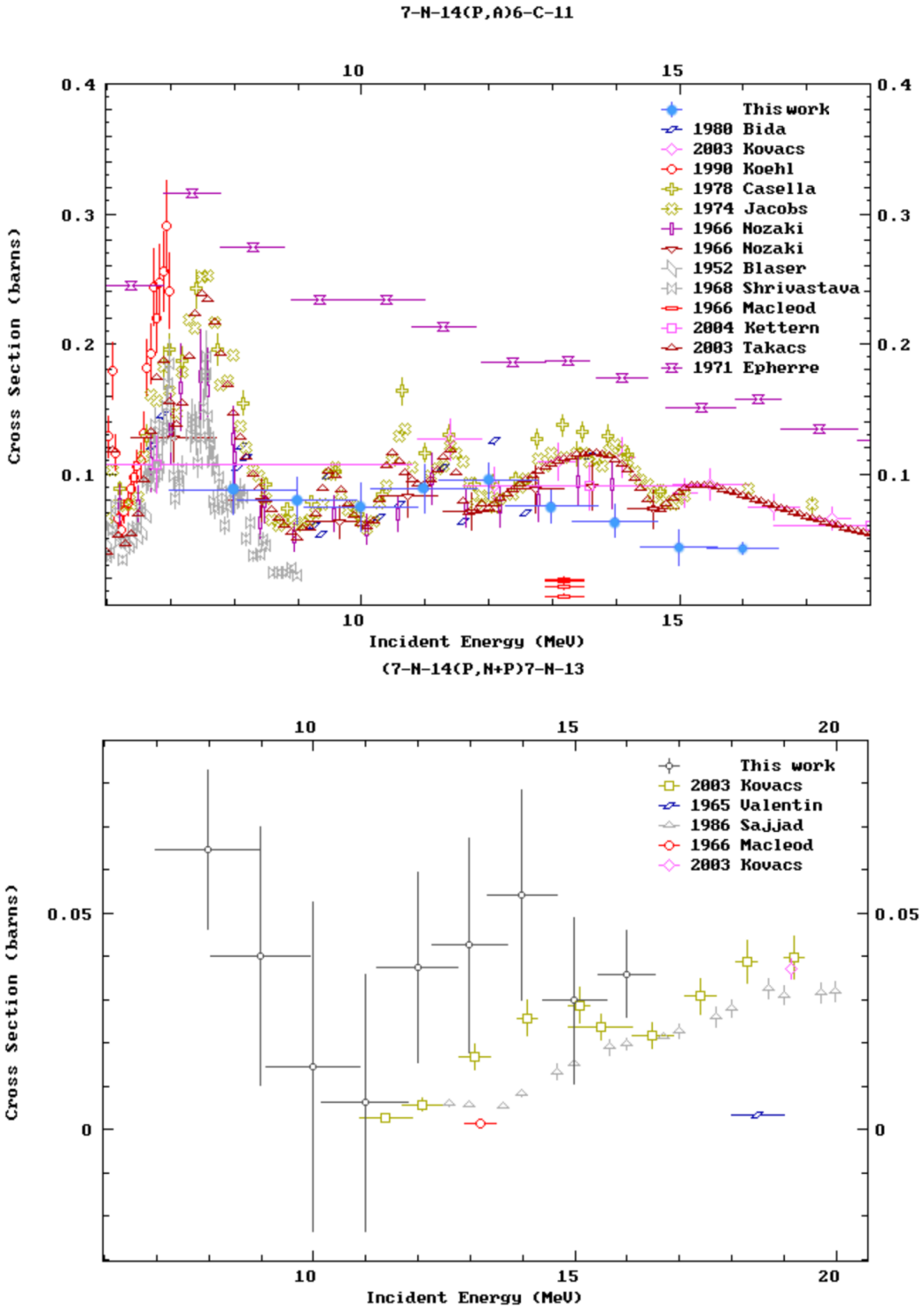

Figure 26: *$^{14}N(p,*)^{11}C$ and $^{14}N(p,*)^{13}N$ cross section comparison between measured data in this work and previous experimental results from EXFOR.*

5 Conclusions and Outlook

The results obtained in the elaboration of this master thesis are a first approach to the measurement of β^+ emitter cross sections at the Centro Nacional de Aceeradors (CNA) with application in range verification in protontherapy. A series of experimental, simulation and analysis tools have been developed for this purpose and used for the first time in this experimental campaing. These include, among others: Geant4 simulations of the beam degradation through matter, an irradiation set-up for thin layers at the cyclotron, a characterization protocol for both NaI and PET detectors, the software required to process the data from the CAEN V1720 digitizer, the ROOT macros for exponential fitting, and a series of algorithms for extracting the cross sections of each reaction from the measured yields in each layer. The main novelty in this experiment with respect to most of the previous ones is that the irradiation of all the layers is done in a single irradiation, while previous works are based on the degradation of the beam to a given energy and the subsequent irradation of a single layer, thus a single data point per irradiation.

The result of this work is a set of experimental cross sections for six different reactions (^{11}C and ^{13}N production in C, O and N) in the energy range betwen 8 and 17 MeV, some of which have been masured for the first time ever (according to what is available in EXFOR). The results are in fair agreement with previous data in the cases where there are several data sets availabe, for instance for ^{16}O(p,*)^{13}N and ^{14}N(p,*)^{11}C. In the other cases there are sizable differences with the few data available.

The possible improvements that have been identified for future experiments are:

- The PET measurements should be longer in order to reach a stable counting rate, thus allowing determining directly the background level.
- In some case, more activity (longer irradiations or higher beam intensities) would help improving the statistics of the decay curves, and thus of the fit coefficients obtained.
- The dependency of the PET efficiency with the position of the layers should be investigated.
- Certified ^{22}Na calibration sources with a lower uncertainty in their activity should be employed.
- The use of gelatenous water for oxigen and Si-N compounds for Nytrogen would eliminate the correlation between the cross sections measured. However, it is not clear if thin layers of these materials can be obtained.

Regarding other future measurements, this project will continue by improving the measurements already performed, and then increasing the energy range (at other facilities available in Europe) and for variety of PET isotopes, including short-lived ones by using a in-room PET at a clinical proton beam facility.

Bibliography

[1] W. D. Newhauser and R. Zhang, "The physics of proton therapy", *Phys. Med. Biol.*, no. 60, p. R155 –R209, 2015.

[2] R. R. Wilson, "Radiological use of fast protons", *Radiology*, vol. 47, no. 5, pp. 487–491, 1946.

[3] J. H. Lawrence *et al.*, "Pituitary irradiation with high-energy proton beams a preliminary report", *American Association for Cancer Research*, vol. 18, no. 2, pp. 121–134, 1958.

[4] R. Kjellberg *et al.*, "Stereotaxic instrument for use with the Bragg peak of a proton beam", *Confinia Neurol.*, vol. 22, 1962a.

[5] R. Kjellberg *et al.*, "The Bragg peak of a proton beam in intracranial therapy of tumors", *Transactions of the American Neurological Association (U.S.)*, vol. 87, 1962b.

[6] E. Gragoudas *et al.*, "Proton beam irradiation of uveal melanomas: Results of 5.5-year study", *Archives of Ophthalmology*, vol. 100, no. 6, pp. 928–934, 1982.

[7] A. M. Koehler *et al.*, "Flattening of proton dose distributions for large-field radiotherapy", *Medical Physics*, vol. 4, no. 4, pp. 297–301, 1977.

[8] "Particle Therapy Co-Operative group (PTCOG)." `https://www.ptcog.ch`.

[9] H. Bethe, "Zur theorie des durchgangs schneller korpuskularstrahlen durch materie", *Ann. Phys.*, no. 5, p. 324–400, 1930.

[10] F. Bloch, "Zur bremsung rasch bewegter teilchen beim durchgang durch materie", *Ann. Phys.*, no. 16, pp. 285–320, 1933.

[11] M. Würl, "Towards offline PET monitoring at a cyclotron-based proton therapy facility. experiments and Monte Carlo simulations", Master's thesis, Ludwig Maximilians Universität (LMU), München, 2015.

[12] H. Paganetti, "Proton beam therapy", in *Proton Beam Therapy*, 2399-2891, pp. 1–1 to 1–23, IOP Publishing, 2017.

[13] K. Parodi, H. Paganetti, *et al.*, "PET/CT imaging for treatment verification after proton therapy: A study with plastic phantoms and metallic implants", *Medical Physics*, vol. 34, no. 2, pp. 419–435, 2007.

[14] H. Paganetti, "Range uncertainties in proton therapy and the role of Monte Carlo simulations", *Phys. Med. Biol.*, vol. 57, no. 11, pp. R99–R117, 2012.

[15] S. Moteabbed, M. España and H. Paganetti, "Monte Carlo patient study on the comparison of prompt gamma and PET imaging for range verification in proton therapy", *Phys. Med. Biol.*, no. 56, p. 1063–1082, 2011.

[16] K. Matsushita *et al.*, "Measurement of proton-induced target fragmentation cross sections in Carbon", *Nuclear Physics A*, no. 946, p. 104–116, 2016.

[17] N. M. Hintz *et al.*, "Excitation Functions to 100 MeV", *Phys. Rev.*, vol. 88, no. 19, 1952.

[18] R. L. Aamodt *et al.*, "^{12}C(p,pn)^{11}C Cross Section from threshold to 340 MeV", *Phys. Rev.*, vol. 88, no. 4, 1952.

[19] B. L. Cohen, "(p, γ) Cross Sections", *Phys. Rev.*, vol. 100, pp. 206–208, 1955.

[20] S. W. Kitwanga *et al.*, "Production of ^{13}N radioactive nuclei from ^{13}C(p,n) or ^{16}O(p,α) reactions", *Phys. Rev. C*, vol. 40, pp. 35–38, 1989.

[21] M. L. Firouzbakht *et al.*, "Cross-section measurements for the ^{13}C$(p, n)^{13}$N and ^{12}C$(d, n)^{13}$N nuclear reactions", *Radiochimica Acta*, vol. 55, 1991.

[22] J. Bair *et al.*, "Neutron yields from the 4–12 MeV proton bombardment of ^{11}B, ^{13}C and ^{18}O as related to the production of ^{11}C, ^{13}N and ^{18}F", *The International Journal of Applied Radiation and Isotopes*, vol. 32, no. 6, pp. 389 – 395, 1981.

[23] T. Akagi *et al.*, "Experimental study for the production cross sections of positron emitters induced from ^{12}C and ^{16}O nuclei by low-energy proton beams", *Radiation Measurements*, vol. 59, pp. 262 – 269, 2013.

[24] S. Takács *et al.*, "Validation and upgrading of the recommended cross section data of charged particle reactions used for production of PET radioisotopes", *Nuclear Instruments and Methods in Physics Research Section B: Beam Interactions with Materials and Atoms*, vol. 211, no. 2, pp. 169 – 189, 2003.

[25] Z. Kovács *et al.*, "Cross section measurements using gas and solid targets for production of the positron-emitting radionuclide o-14", *Radiochimica Acta*, vol. 91, 2003.

[26] M. Sajjad *et al.*, "Excitation functions for the ^{16}O(p,α)^{13}N and ^{14}N(p,pn)^{13}N reactions", *Radiochimica Acta*, vol. 39, p. 165, 1986.

[27] "Experimental nuclear reaction data (EXFOR)." `https://www-nds.iaea.org/exfor/`.

[28] S. M. Qaim, "Nuclear data for production and medical application of radionuclides: Present status and future needs", *Phys. Med. Biol.*, no. 44, p. 31–49, 2017.

[29] "Centro Nacional de Aceleradores (CNA)." `http://acdc.sav.us.es/cna/`.

[30] "Geant 4." `https://geant4.web.cern.ch/geant4/`.

[31] J. F. Ziegler, "The stopping and range of ions in matter." `http://www.srim.org/`.

[32] CERN, "ROOT. Data Analysis Framework." `https://www.root.cern.ch`.

[33] K. Kettern *et al.*, "Formation of short-lived positron emitters in reactions of protons of energies up to 200 MeV with the target elements carbon, nitrogen and oxygen", *Applied Radiation and Isotopes*, vol. 60, no. 6, pp. 939 – 945, 2004.